**Forsterite Surfaces as Models of Interstellar Core Dust Grains: Computational Study of Carbon Monoxide Adsorption**

(Article begins on next page)

# Forsterite surfaces as models of interstellar core dust grains: computational study of carbon monoxide adsorption

Lorenzo Zamirri, Marta Corno, Albert Rimola, and Piero Ugliengo

## Just Accepted

# Forsterite surfaces as models of interstellar core dust grains: computational study of carbon monoxide adsorption

*Lorenzo Zamirri[1], Marta Corno[1#*], Albert Rimola[2] and Piero Ugliengo[1*]*

[1]Dipartimento di Chimica and NIS – Nanostructured Interfaces and Surfaces – Centre, Università

degli Studi di Torino, via P. Giuria 7, 10125, Torino, Italy

[2]Departament de Química, Universitat Autònoma de Barcelona, 08193 Bellaterra, Spain

*Corresponding authors; piero.ugliengo@unito.it, telephone:+390116704596.

marta.corno@uniupo.it, telephone: +390131360418

#Present address: Dipartimento di Scienze e Innovazione Tecnologica, Università del Piemonte Orientale, Viale Teresa Michel 11, 15121 Alessandria, Italy

## Abstract

Carbon monoxide (CO) is the second most abundant gas-phase molecule after molecular hydrogen ($H_2$) of the Interstellar Medium (ISM). In Molecular Clouds (MCs), an important component of the ISM, it adsorbs at the surface of core grains, usually made of Mg/Fe silicates, and originates Complex Organic Molecules (COMs) through the catalytic power of active sites at the grain surfaces. To understand the atomistic, energetic and spectroscopic details of the CO adsorption on core grains, we resorted to Density Functional Theory based on the hybrid B3LYP-D* functional inclusive of dispersion contribution. We modeled the complexity of interstellar silicate grains by studying adsorption events on a large set of infinite extended surfaces cut out from the bulk $Mg_2SiO_4$ forsterite, the Mg end-member of olivines ($Mg_{2x}Fe_{2-2x}SiO_4$), also a very common mineral on Earth crust. Energetic and structural features indicate that CO get exclusively physisorbed, with binding energy values in the 23-68 kJ $mol^{-1}$ range. Detailed analysis of data revealed that dispersive interactions are relevant together with the important electrostatic contribution due to the quadrupolar nature of the CO molecule. We performed a full thermodynamic treatment of the CO adsorption at the very low temperature typical of the ISM as well as a full spectroscopic characterization of the CO stretching frequency, which we prove to be extremely sensitive to the local nature of the surface-active site of adsorption.

We also performed a detailed kinetic analysis of CO desorption from the surface models at different temperatures characterizing the colder regions of the ISM. Our computed data could be incorporated in the various astrochemical models of interstellar grains developed so far and thus contribute to improve the description of the complex chemical network occurring at their surfaces.

*Key words*

## 1. Introduction

The observation of the Interstellar Medium (ISM) by means of rotational spectroscopic techniques was performed since the first half of the XX century, and has revealed, according to the Cologne database,[1] the presence of more than 200 molecular species in the Molecular Clouds (MCs).[2,3] These observations suggested the occurrence of different chemical processes with prebiotic implications, which are ultimately connected with the emergence of life on Earth (and maybe on other exogenous planets) since MCs are the cradle where star-forming processes occur. Moreover, the Solar System not only includes the presence of comets, asteroids and Kuiper belt-objects, but also suffers from a dust flux coming from the remote ISM. This dust is continuously falling on Earth with a density of about $10^{-6}$ $m^{-3}$.[4] Specifically, one hypothesis is that amino acids precursors, or even amino acids themselves, can form in MCs under suitable conditions. As an example, aminoacetonitrile $H_2NCH_2CN$, the precursor of glycine, was identified in Sgr B2, a giant MC localized at the center of the Milky Way.[5]

The IR observations of MCs have also suggested the presence of a small fraction of solid, dust-like material whose exact composition is still a current matter of debate.

IR telescope observations support the presence of solid materials in MCs. The 9.7 $\mu$m and 18 $\mu$m absorption bands are particularly important as they are associated with the Si-O stretching and O-Si-O bending modes, suggesting the presence of silicates, mainly olivines $Mg_{2x}Fe_{2-2x}SiO_4$.[6] The broadness of these two features leads to hypothesize that the structure of such grains is dominated by an amorphous phase, although it is also speculated that ~ 5% of the grain population is crystalline, and in other environments (*e.g.*, circumstellar and protostellar disks, comets and interplanetary medium) even greater.[7,8] Moreover, crystalline silicates are expected to be larger in size than amorphous ones and could have formed through coagulation of smaller particles.[8] In MCs, these two class of refractory materials are covered in ice mantles which are built up by the freeze-out of gas-phase species, and also by the *in-situ* formation of molecules, on the cold dust grain surfaces. The composition of the ices can be elucidated by their infrared spectroscopic features.[9] In

general, $H_2O$ is the most abundant constituent of the mantles, which is clearly featured by its 3.0 $\mu$m and 6.00 $\mu$m bands associated with the O-H stretching and H-O-H bending modes. Nonetheless, mantles also contain other species, and hence that they are also usually referred to as "dirty ices"; *i.e.*, CO (4.67 $\mu$m), $CO_2$ (4.27 and 15.2 $\mu$m), $CH_3OH$ (3.54 and 9.75 $\mu$m), $NH_3$ (2.97 $\mu$m) $CH_4$ (7.68 $\mu$m), $H_2CO$ (5.81 $\mu$m).[10]

Since H is the most abundant species in the ISM, the actual composition of a particular ice mantle depends on the $H/H_2$ ratio where it is formed. In regions where this ratio is greater than 1, reactive species such as O, N and C are readily hydrogenated thus forming hydride-rich ices (*i.e.*, $H_2O$, $NH_3$ and $CH_4$). In contrast, if the $H/H_2$ is significantly less than 1, the reactive species are free to interact with other species forming molecules such as CO, $CO_2$ or $N_2$.Thus, two qualitatively different types of ice matter can be produced: with high or with low dipole moment species, usually referred to as polar or apolar ices, respectively.[11] It is worth mentioning that even in the apolar ices, $H_2O$ is a prominent species at least in the very first layers covering the silicate core, which are expected to be composed by hydrogenated species.[9,12] For these apolar ices, CO is usually the second most abundant solid phase species,[11] even if it has been reported that around some sources, solid CO becomes the most abundant species (up to 85% with respect to solid $H_2O$).[9] The CO IR features in ices with high percentages of CO are perturbed by interaction with other apolar species (e.g., $CO_2$) and not by $H_2O$ thus suggesting the formation of apolar islands within the ice mantle.[9] In our opinion, such great abundances (with respect to $H_2O$) together with the fact that CO is the second most abundant gas-phase species could justify a theoretical investigation of the interaction between CO molecules and olivines surfaces.

Grain surfaces have also a role of paramount importance in the chemical evolution of space: they can act as catalysts in the formation of both simple and more evolved molecular species, including the Complex Organic Molecules (COMs). For example, there is general consensus that $H_2$, the most abundant species in the Universe, can form at these surfaces and not via symmetry-prohibited, direct gas-phase collision reactions.[13] Formation of COMs, such as carbonyl species, alcohols or

even amino acids precursors would occur by involving other simple but reactive molecules such as carbon monoxide (CO), the second most abundant gas-phase species in the ISM.[2] Hence, a detailed study of the mechanisms underlying the interaction of (covered) silicate grains and CO may improve our knowledge about the chemical processes occurring in MCs.

Laboratory experiments[14–23] can hardly reproduce the MCs physical features (very low temperatures and atomic densities), thus Quantum-Mechanical (QM) methods represent a powerful alternative to simulate chemical processes occurring in MCs. A comprehensive knowledge of olivine surface energetics and morphology at the atomic level is of extreme importance to understand the true nature of these processes and, more generally, all processes involving the olivine interface. Several studies at different computational level have been conducted in order to investigate possible formation, adsorption and desorption of small organic and inorganic molecules such as ammonia,[24] glycine,[24] carbon dioxide,[25] hydrogen,[13,26–31] water.[24,25,32–40] Only a few of them have dealt with the problem of olivine's morphology[41–46] together with a complete QM level of treatment.[13,43–46] Furthermore, to the best of our knowledge, no theoretical works dealing with the adsorption of CO on olivine surfaces can be found in the literature.

For these reasons, in this work, we have modeled the adsorption of CO on the end-member of olivine, *i.e.* crystalline forsterite ($Mg_2SiO_4$) surfaces by means of the Density Functional Theory (DFT), aiming to contribute to the understanding of interstellar gas-grain phenomena by providing a reliable theoretical background. We assume a crystalline nature of the interstellar grain core, well aware that the dominant phase is amorphous. Obviously, when compared to the unknown nature of amorphous silicate grain structure, crystalline models ensure a well-defined structure derived from the bulk silicate. We hope that this work can be useful to elucidate processes occuring at silicate surfaces in the very harsh condition characterizing the various regions of the ISM. Important progress in the modeling of amorphous grains, albeit of very small size, is the work leaded by S. Bromley.[47]

## 2. Computational Details

We performed all calculations with a developmental version of the periodic computational code CRYSTAL14[48] and we only report the most relevant details leaving the more specific ones in the Supporting Information (SI). We used the hybrid B3LYP Hamiltonian,[49–51] already shown to provide accurate results for the structural and dynamical properties of olivine end-members.[52–55] To account for dispersion forces, in this work we used the D* version, which is a modified Grimme's D2 version,[56–58] optimized for the B3LYP functional in molecular crystals by Civalleri et al.[59]

CRYSTAL adopts Gaussian based functions and we used the same Gaussian-type basis set applied by Bruno et al.[45] for forsterite bulk and slabs, while CO was dressed by the Alhrichs-TZV polarized basis sets (details in SI).[60]

We adopted default values for the energetic thresholds controlling the accuracy in the evaluation of the Coulomb and exchange integrals. We used an extra-large grid to ensure a satisfactory accuracy in the numerically integrated electron charge density, as previously stated by Bruno et al[45] and enough $k$ sampling points to sample the Brillouin zone to ensure a good energy convergence (see SI).

Geometry optimizations of bulk and slabs adducts (forsterite surfaces + CO molecules) were performed following the Broyden-Fletcher-Goldfarb-Shanno (BFGS) algorithm[61–64] and allowing only the atomic positions to relax (cells parameters were kept fixed to bulk values reported by Bruno).[45] Symmetry was enforced during the bulk optimization only.

To assess the relative stability of the seven surface models, the surface energies $E_S$ were computed as

$$E_S = \frac{E_{slab} - 4E_{bulk}}{2A} \qquad \text{Eq. 1}$$

where $E_{slab}$ and $E_{bulk}$ are the DFT unit cell total energies. For a more detailed discussion on how to compute $E_S$, the interested reader can refer to a previous work on surface modelling of bio-ceramics.[65] The factor 4 accounts for the stoichiometric 4:1 ratio between slab and bulk.

For the optimized adduct structures, we computed the binding energies per adsorbed CO (BE), including dispersion and corrected for the Basis Set Superposition Error (BSSE)[66,67] through the "Counterpoise" method (CP),[68] as detailed in the SI.

On the optimized adduct structures, we restrict the calculation of the harmonic IR spectrum in $\Gamma$ point[69,70] to the CO molecule considered as a fragment (the surface/CO intermolecular modes are included) by diagonalizing the mass-weighted Hessian matrix.[69] This strategy has been validated by our research group in the past and showed to be satisfactory.[71,72] The IR intensity of each normal mode of vibration was computed using the Berry phase approach.[73]

We scaled all frequencies values by the following scaling factor $s_{fac}$, derived by comparing the B3LYP harmonic frequency value for the isolated CO with the experimental one for CO in gas phase:

$$s_{fac} = \frac{\bar{v}_{exp} \, (free \; CO)}{\bar{v}_{theo} \, (free \; CO)} = \frac{2143 \; cm^{-1}}{2201 \; cm^{-1}} = 0.9736 \qquad \text{Eq. 2}$$

This partially recovers the systematic errors associated with B3LYP method and corrects for anharmonicity, improving the comparison with experiment. For each optimized structure $i$, we computed the IR spectrum $S_i(\bar{v})$ in the CO stretching region as a linear combination of Gaussian functions $G(\bar{v} - \bar{v}_j)$, each one centered at the $j$-th CO B3LYP scaled frequency value $\bar{v}_j$. We arbitrarily chose a value of 15 cm$^{-1}$ as Full Width at Half-Maximum (FWHM). Finally, we weighted each band $j$ by the corresponding IR intensity ($I_j$):

$$S_i(\bar{v}) = \sum_j I_j G(\bar{v} - \bar{v}_j) \qquad \text{Eq. 3}$$

The frequencies computed for the CO fragment allowed computing the desorption enthalpies variations at 0 K, through the standard statistical thermodynamics relation:

$$\Delta_{des}H(0) = -\Delta_{ads}H(0) = BE - \Delta ZPE \qquad \text{Eq. 4}$$

where ΔZPE is the Zero-Point Energy correction. We neglect the $PV$ and the thermal factor terms,[13] which, at the typical pressure characterizing MCs, are completely negligible.[74] Therefore, Gibbs free energies coincide with Helmholtz free energies $\Delta_{ads}A$

$$\Delta_{ads}A(T) = -\text{BE} + \Delta\text{ZPE} + \Delta E(T) - T\Delta S(T) \qquad \text{Eq. 5}$$

We outline that $\Delta\text{ZPE}$, $\Delta E(T)$ and $\Delta S(T)$ terms are evaluated only for the adsorbed CO molecules (see *Surface free energies and adsorption free energies (Eq. 7 and 8)* section of the SI for a complete justification).

We used the computed binding energies to evaluate desorption times ($t_{des}$) using Eyring equation. Thus, desorption times resulted as:

$$t_{des} = \frac{1}{k_D} = \frac{h}{k_B T} e^{-\Delta_{ads}A/RT} \qquad \text{Eq. 6}$$

To evaluate the stability of the surfaces in presence of adsorbed carbon monoxide, we computed the surface free energies $G_S$ according to the following expression:

$$G_S(T, P, \sigma) = E_S + \Delta\bar{\bar{G}}(T, P^\theta, \sigma)_{CO} - \sigma\left[\text{BE} + RT\ln\left(\frac{P}{P^\theta}\right)\right] \qquad \text{Eq. 7}$$

which is derived from first principle thermodynamics.[75–85] $E_S$ is the surface energy computed according to Eq. 1, BE is the dispersion-BSSE-corrected binding energy per adsorbed molecule. $T, P$ and $P^\theta$ are the absolute temperature, the partial pressure of CO and the standard pressure (= 101 325 Pa). $\sigma$ is the surface density, *i.e.* the number $n^\dagger = n/2$ of adsorbed CO molecules per unit cell divided by the unit area $A$ of the slab ($n$ total number of adsorbed CO molecules on both ends of the slab model). In $\Delta\bar{\bar{G}}(T, P^\theta, \sigma)_{CO} = \Delta G(T, P^\theta, n)_{CO}/2A$, $\Delta G(T, P^\theta, n)_{CO}$ is the Gibbs's free energy correction for gaseous CO computed from statistical thermodynamics relations.

From Eq. 7, Gibbs's free energy of CO adsorption becomes:

$$\Delta_{ads}G(T, P, n) = \Delta G(T, P^\theta, n)_{CO} - n\left[\text{BE} + RT\ln\left(\frac{P}{P^\theta}\right)\right] \qquad \text{Eq. 8}$$

Both Eq. 7 and 8 are based on the assumption of thermodynamic equilibrium among phases.[79–82] For a detailed discussion, see the SI.

## 3. Results and discussion

*3.1 Forsterite surface models characterization*

To start with, we borrowed both the forsterite bulk and surface models from Bruno et al.[45] previous

work at B3LYP (without Grimme's correction for dispersive interactions) level of theory of the

most natural occurring forsterite surfaces, *i.e.* (010), (120), (101), (001), (111), (021) and (110). We

re-optimized at B3LYP-D* level only the atomic positions keeping the cell parameters computed by

Bruno et al. Results are summarized in Table 1, together with the experimental data[86] and computed

ones obtained by Escamilla-Roa at PBE level.[24]

**Table 1.** Experimental and computed lattice parameters (Å) for forsterite bulk. The present work adopts the same cell parameters of Bruno et al. work.[45] Percentage variations with respect to experimental values in parentheses.

| Parameter | Experimental[#] | Escamilla-Roa[$] | Bruno[§]/This work (%Δ) |
|---|---|---|---|
| *a* | 4.7490 | 4.81(1.3%) | 4.7892 (0.8%) |
| *b* | 10.1985 | 10.35(1.5%) | 10.2539 (0.5%) |
| *c* | 5.9792 | 6.06(1.4%) | 6.0092 (0.5%) |

[#]: Bostom.[86]

[$]: Escamilla-Roa et al.[24]

[§]: Bruno et al.[45]

The models representing the seven surfaces (slab models) have resulted by properly cutting the

optimized bulk structure, following the slab model approach, *i.e.* without generating a perpendicular

dipolar moment,[87] or breaking the unity of the $SiO_4$ moiety, in agreement with previous

computational works showing forsterite as an ionic material where the $SiO_4$ groups act as single

anion entity.[24,32–36,39,88–90] For a detailed discussion of how slabs models have been generated, see

the original Bruno's work.[45] With local Gaussian basis set, there is no need to replicate the slab

along the *c* axis, as mandatory when adopting plane waves basis set. In this work we followed the

same computational scheme by Bruno and coworkers, by further adding the Grimme's corrections

for dispersive interactions,[56–58] as detailed in the Computational section. In practice, from the

optimized slab structures, we computed the surface energies, the morphological relevance index

(MRI, *i.e.* the ratio, expressed as percentage, between the unit area of a single surface and the total

area of the crystal) and, through the Wulff theorem,[91] the equilibrium shape (ES) of the crystal a 0

K (Table 2 and Figure 2).

Figure 1 shows the structural features of forsterite bulk and slabs. Forsterite ($Mg_2SiO_4$), the Mg

end-member of the olivines isomorphic solid solution $(Mg,Fe)_2SiO_4$, belongs to *Pbnm* space group

(orthorhombic, Z=4, $a \neq b \neq c$, $\alpha = \beta = \gamma = 90.0°$). Its bulk structure is composed of a distorted

hexagonally close-packed array of oxygen with 1/8 of the tetrahedral sites occupied by $Si^{4+}$ ($SiO_4$

units) and 1/2 of the octahedral sites occupied by divalent cations ($Mg^{2+}$) usually denoted as M1 and

M2 ($MgO_6$ units). Of the two octahedral sites, the M1 site, which is more distorted and compact

than M2 one, forms edge-sharing chains parallel to the *c* axis. The adsorption surface sites for all

the seven slab models are either $Mg^{2+}$ cations or oxygen atoms belonging to external $SiO_4$ groups.

We labeled each site in alphabetic order following its *z*-coordinate value, from the most (highest *z*-

coordinate) to the least (lowest *z*-coordinated) exposed (see Figure 1), in which the *z*-coordinate

refers to the Cartesian axis perpendicular to the cut plane.

The seven surfaces are characterized by very different structural features (Table 2) and

morphologies: some surfaces, such as the (010) and the (001) ones, show very compact structures

with only a few exposed sites and very little surface area values, while others such as the (120), the

(101), and the (111) ones present irregular morphologies, thus exposing several adsorption sites.

Finally, the last two surfaces, (021) and (110), are characterized by very low-coordinated sites (Mg

A for the first one and Mg A and Mg B for the second one) explaining their high surface energies

(Table 2). The considered slab models did not exhibit defects, such as steps, corners, and vacancies.

Nevertheless, as reported by King et al.[36] for the water case, the energetics adsorption process is not

influenced by such defects, but, rather, by the presence of exposed and low-coordinated Mg cations.
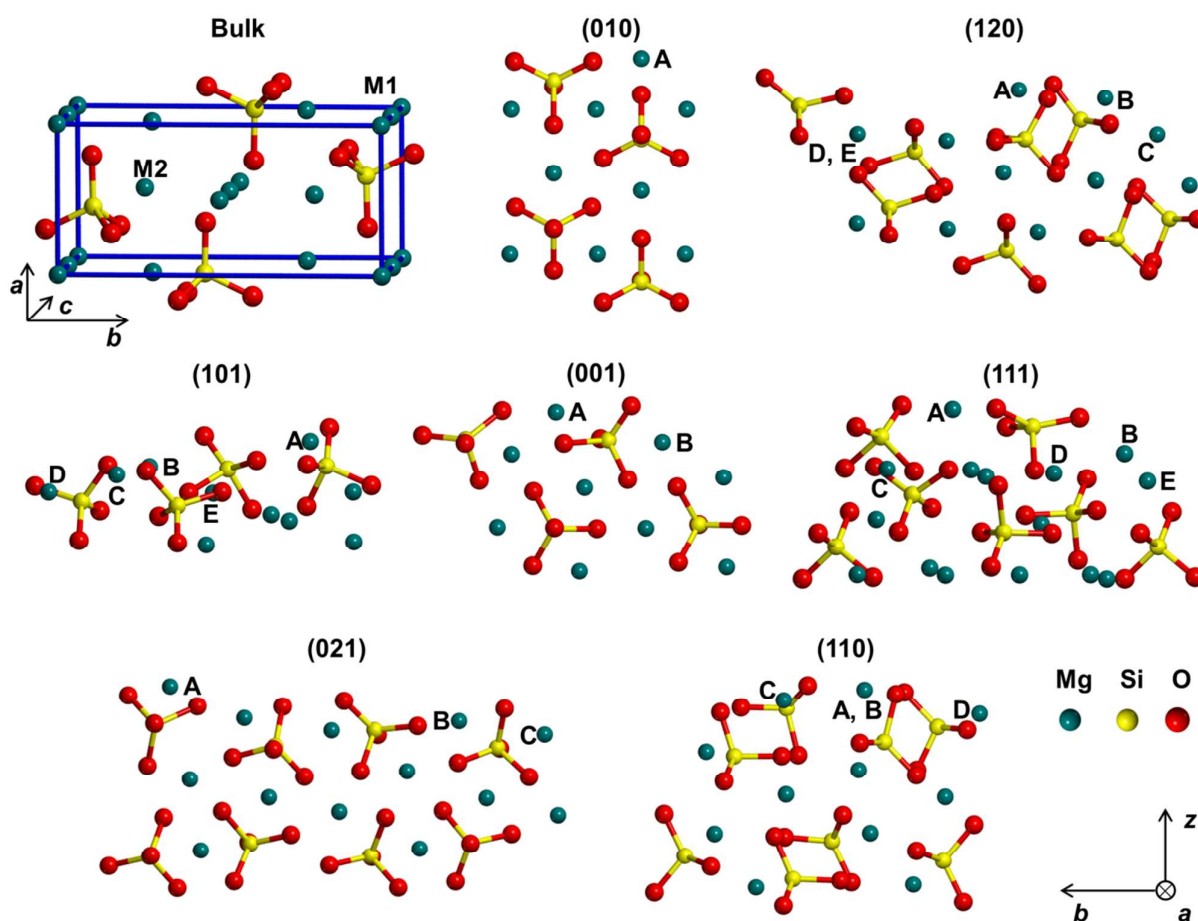
**Figure 1.** Forsterite bulk (top-left corner, unit cell borders in blue) and side views of the seven slab models. M1 and M2 indicate the Mg octahedral sites. The figure only shows few atomic layers, for sake of clarity. Mg cations available for adsorption are labeled in alphabetic order according to their $z$-coordinated. For the (120) and (110) surfaces, Mg D/E and Mg A/B are indicated as "D,E" and "A,B", respectively, since they are eclipsed in this representation.

The surface energy values $E_S$ (at 0 K) according to Eq. 1 (Table 2) allow sorting the seven surfaces by their relative stability: the higher the surface energy, the less stable is the surface. Table 2 highlights the role of dispersion interaction on the $E_S$ values by comparing the B3LYP-D* data with the ones computed at B3LYP//B3LYP-D* (in parentheses), *i.e.* by single point energy evaluation at B3LYP on the B3LYP-D* optimized geometries. This comparison gives a measure of the role of dispersion on the final $E_S$ values. The stability order, at B3LYP//B3LYP-D*, is:

$$(010) < (120) < (101) < (001) < (111) < (021) < (110)$$

with the (010) being the most stable one. Data at B3LYP-D* follow the same order of stability, which also coincides with that computed by Bruno et al. (Table 2). To compute the MRI values and

the resulting equilibrium crystal morphology at 0 K (Figure 2) we used the $E_S$ values from B3LYP-D*.

**Table 2.** Structural and energetic features for the seven slab models. Cell parameters, $a$, $b$ and $\gamma$ (Å, degrees), $A$ (Å$^2$) surface unit cell area, $E_S$ (J m$^{-2}$) surface energy from Eq. 1 (values at B3LYP//B3LYP-D* in parentheses) and Morphological Relevance Index (MRI, see text for details). %Δ is the percentage variations between Bruno's and the present B3LYP//B3LYP-D* values. The MRI for the present work is for $E_S$ at B3LYP-D*

| (hkl) | Cell parameters | | | | $E_S$ | | | MRI | |
|---|---|---|---|---|---|---|---|---|---|
| | $a$ | $b$ | $\gamma$ | $A$ | This work | Bruno[§] | %Δ | This work | Bruno[§] |
| (010) | 4.795 | 6.043 | 90.0 | 28.98 | 1.44 (1.23) | 1.22 | 0.8 | 23.8 | 21.7 |
| (120) | 6.009 | 13.932 | 90.4 | 83.71 | 1.68 (1.37) | 1.36 | 0.7 | 29.7 | 37.0 |
| (101) | 7.745 | 10.253 | 90.1 | 79.41 | 1.96 (1.62) | 1.78 | −9.0 | 20.7 | 12.2 |
| (001) | 4.806 | 10.149 | 91.0 | 48.76 | 1.98 (1.72) | 1.78 | −3.4 | 19.8 | 15.8 |
| (111) | 7.684 | 11.147 | 105.1 | 82.70 | 2.19 (1.83) | 1.84 | −0.5 | 2.5 | 8.2 |
| (021) | 4.828 | 15.650 | 89.7 | 75.55 | 2.24 (1.91) | 1.90 | 0.5 | 3.5 | 5.1 |
| (110) | 6.105 | 11.062 | 90.0 | 67.53 | 2.46 (2.17) | 2.18 | −0.5 | 0.0 | 0.0 |

§: Ref.[45]

The B3LYP//B3LYP-D* $E_S$ percentage variations from the present work compared to that by Bruno et al.[45] are relatively small for all cases but for (101) and (001) surfaces, probably due to large structural rearrangements occurring during the optimization when dispersion is included. When dispersion is fully accounted for at B3LYP-D* level the corresponding MRI values are significantly different from that by Bruno et al.[45] Nevertheless, the final equilibrium shape morphologies only show relevant change in surface extension for the (101) and (111) facets, the ones whose $E_S$ is affected most by the inclusion of dispersion (Figure 2).
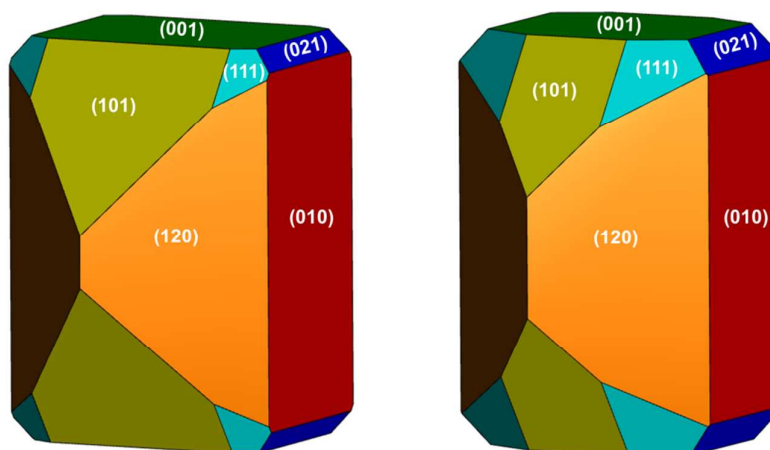
**Figure 2.** Comparison between the Equilibrium Shape (ES) at 0 K of crystalline forsterite from the Wulff's construction,[91] by using surface energy values from the present work (inclusive of dispersion, left) and from Bruno's work[45] (right, Table 2). Surfaces RGB color scale from the most (red) to the least (blue) stable. Picture created with VESTA software.[92]

To characterize the forsterite surfaces with respect to CO interaction, we also computed the electrostatic potential maps (ESPMs) superimposed to the ground state electron density (Figure 3). For transition metals, the CO/surface interaction is dominated by chemical effects ($\pi$-back-donation),[93–95] while for ionic systems, like the present case, where chemical effects are very small, electrostatic complementarity between CO and the adsorbing surface docks CO at the different sites.[96,97] Figure 3 clearly shows the quadrupolar nature of CO, which is dominant over its small dipole moment, with a deeper negative value around C atom compared to oxygen, in agreement with previous findings.[98] Within B3LYP-D* approach, the CO dipole has the right alignment ($C(\delta^-) \rightarrow O(\delta^+)$) with magnitude of 0.094 D, slightly smaller than the experimental value of 0.122 D.[99] Figure 3 also displays deep positive and negative regions over the Mg and the $SiO_4$ ions, for two representative forsterite surfaces. Clearly, the complexity of the surface ESPMs, the quadrupolar nature of the CO, together with the role played by the dispersion interactions - not accounted for by the ESPMs - hinder an easy prediction of the final CO/surface configuration without actually running the full calculation. Nevertheless, guided by the principle of electrostatic complementarity, we started with up to 37 different CO/surface cases for all seven forsterite surfaces. For each case, full geometry optimization at B3LYP-D* reveal the subtle structural and energetic details of this kind of interaction.
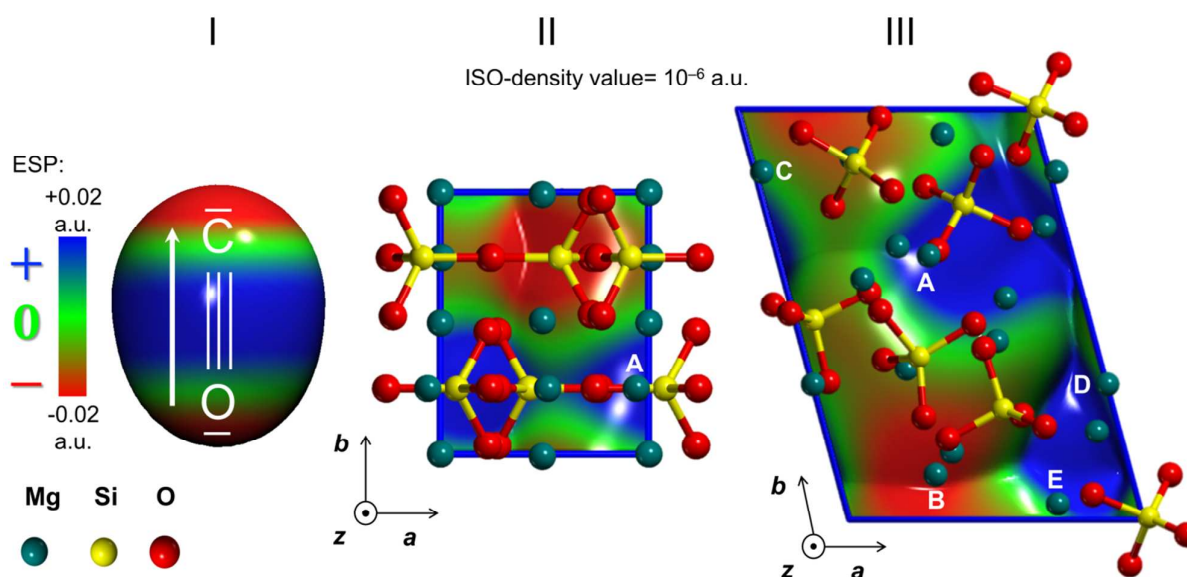
**Figure 3.** B3LYP-D* electrostatic potential maps (ESPMs) superimposed to the ground state electron densities. The ISO-density value for the electron density is equal to $10^{-6}$ a.u. Color code for the ESP: blue = +0.02 a.u., green = 0.0 a.u. and red = –0.02 a.u. I. CO dipole (with arrow) superimposed on the CO ESPM. II. Unit cell top views of the (010) surface superimposed on the ESPM. III. Unit cell top views of the (111) surface superimposed on the ESP map: Mg sites are labeled in alphabetic order from the most (A) to the least exposed (E).

*3.2 CO adsorption on forsterite surfaces*

We started by adsorbing CO molecules at about 2.2 Å from the exposed Mg ions at both the upper/lower surfaces. For all the surfaces, we first considered the lowest CO coverage, by adsorbing a single CO molecule on each Mg available ion, to probe them separately. We then considered the highest CO coverage by adsorbing the CO molecule on all available exposed Mg ions at the same time. For the (120), (101), (001) and (111) surfaces we also tested intermediate coverages. We label all simulated structures according to the Mg ions where CO molecules have been initially located.

For the optimized structures, we computed the average binding energies, BE, *i.e.* the binding energy *per* adsorbed CO molecule and the enthalpies of desorption at 0 K, $\Delta_{des}H(0)$. The computed BE values include deformation, lateral interactions between adsorbed CO molecules[100] and also the Counterpoise correction[68] to cure the basis set superposition error.[66,67] Table 3 resumes the binding energy and enthalpy variation values (Eq. 4) for all the considered cases.

Figure 4 shows, as an example, four significant cases corresponding to the optimum structures of

mono-, intermediate- and maximum CO coverage (see SI for the whole set of cases). In all four

cases, the Mg-C distances (from 2.1 to 2.8 Å) and the energetic features (some tens of kJ mol$^{-1}$)

revealed a weak CO/forsterite interaction, entirely dominated by non-chemical interactions.

Figure 4.I shows that CO molecules do not lie perpendicular to the forsterite surfaces, as in a

classical cation/dipole interaction. For the "(111) 1A" case, CO molecules lie almost flat to the

surface due to the role played by the complex CO quadrupolar/surface ESP interaction and

dispersion interaction.
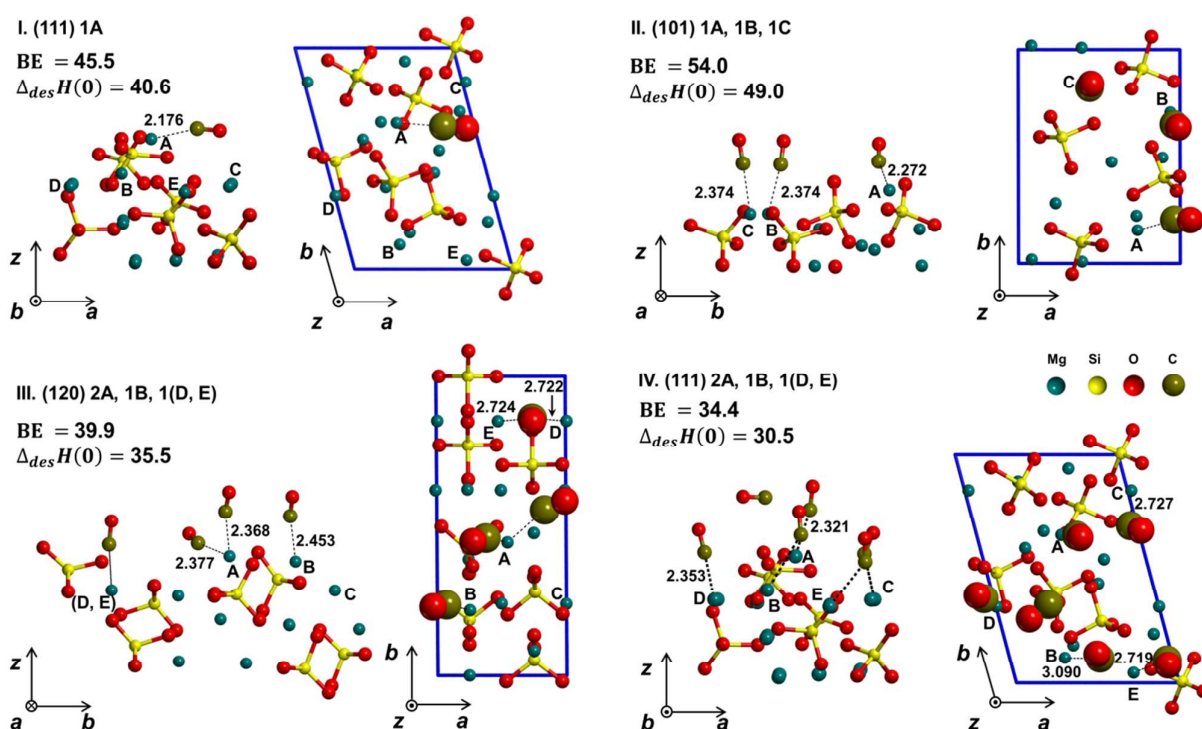


**Figure 4.** Optimized structures for the CO adsorption on three selected forsterite surfaces corresponding to mono (I), intermediate (II) and maximum (III and IV) CO coverages. IV. Maximum coverage for the (111) surface: one of the two molecules initially placed close to Mg A lies parallel to the surface (no Mg-C interactions). Left part: side views, right part: top views. Mg-C distances in Å, BE and $\Delta_{des}H(0)$ in kJ mol$^{-1}$. In top views, CO molecules as van der Waals spheres.

For the "(101) 1A, 1B, 1C" case (intermediate coverage), the CO molecules adsorbed on Mg B and

C lie almost perpendicular to the surfaces, suggesting that in such cases the dipole-charge

interactions dominate. This complex structural scenario will affect the CO stretching frequency in a

rather subtle way (see next section).

Along the route of increasing the CO coverage, we adsorbed two CO molecules on the most

exposed site of the (120), (101), (001) and (111) surface. In all cases, the two CO molecules

repelled themselves. Nevertheless, for the (120), (101) and (001) surfaces, the interaction with the

cation overcomes the repulsion, resulting in structures exhibiting two adsorbed CO molecules *per*

Mg cation (example: Figure 4.III). For the (120) and the (110) surfaces, the closeness of the two Mg

sites (Mg D and E and Mg A and B - respectively - Figure 1 and 4.III but also Figures S3, S8, S11,

S16 of the SI) gives one CO molecule to be bi-coordinated.

**Table 3.** Structural and energetic features of CO adsorbed on forsterite surfaces. Binding energies – corrected for the BSSE – inclusive (BE disp) and non-inclusive (BE no-disp) of Grimme's correction, desorption enthalpy variations $\Delta_{des}H(0)$, lateral interaction energies $E_L$ among CO molecules, BSSE and dispersion (disp) contributions to BEs disp values in kJ mol$^{-1}$; average Mg-C distances $\langle d_{Mg-C} \rangle$ in Å. All energy quantities (3$^{rd}$÷8$^{th}$ columns) are *per* adsorbed CO molecule. Averages, standard deviations (Std. dev.), minimum and maximum values for each quantity are also reported.

| (*hkl*) | Case | BE disp | BE no-disp | $\Delta_{des}H(0)$ | –BSSE | –disp | $E_L$ | $\langle d_{Mg-C} \rangle$ |
|---------|------|---------|------------|-----------|-------|-------|-------|------------|
| (010) | 1A | 44.1 | 24.3 | 39.6 | 28.5 | 19.8 | -0.1 | 2.365 |
| | 1A | 65.0 | 46.5 | 60.2 | 24.3 | 18.5 | -0.5 | 2.332 |
| | 1B | 24.5 | 10.8 | 20.5 | 22.7 | 13.7 | -0.1 | 2.455 |
| | 1C | 35.5 | 11.1 | 31.0 | 27.2 | 24.4 | -0.2 | 2.465 |
| (120) | 1A 1B | 45.8 | 29.7 | 41.4 | 22.4 | 16.1 | -0.3 | 2.380 |
| | 1A 1C | 50.4 | 28.8 | 45.7 | 25.8 | 21.5 | -0.3 | 2.397 |
| | 2A 1B | 40.1 | 22.5 | 35.6 | 20.1 | 17.6 | -0.7 | 2.409 |
| | 1A 1B 1(D,E) | 43.2 | 23.4 | 38.9 | 25.0 | 19.7 | 0.0 | 2.553 |
| | 2A 1B 1(D,E) | 39.9 | 20.1 | 35.5 | 22.4 | 19.8 | -0.2 | 2.529 |
| | 1A | 68.1 | 49.8 | 63.2 | 21.2 | 18.3 | -0.3 | 2.350 |
| | 1B | 43.5 | 24.8 | 38.1 | 26.2 | 18.7 | -0.1 | 2.284 |
| (101) | 1C | 32.5 | 18.9 | 28.1 | 21.2 | 13.6 | -0.1 | 2.394 |
| | 1A 1B 1C | 54.0 | 36.3 | 49.0 | 24.1 | 17.7 | -0.3 | 2.340 |
| | 2A 1B 1C | 45.3 | 27.2 | 40.7 | 22.1 | 18.1 | -0.6 | 2.406 |
| | 1A 1B 1C 1D 1E | 42.5 | 20.7 | 37.7 | 21.7 | 21.8 | -0.3 | 2.447 |
| | 1A | 52.7 | 30.4 | 48.1 | 29.8 | 22.3 | -0.2 | 2.334 |
| | 1B | 43.5 | 26.3 | 38.9 | 28.2 | 17.2 | -0.3 | 2.409 |
| (001) | 1A 1B | 47.8 | 24.1 | 43.0 | 28.1 | 23.8 | -0.2 | 2.557 |
| | 2A 1B | 49.6 | 26.9 | 44.6 | 24.0 | 22.6 | *0.3* | 2.589 |
| | 2A 2B | 23.3 | 0.6 | 18.3 | 19.6 | 22.7 | **-4.7** | 2.354 |
| | 1A | 45.5 | 17.0 | 40.6 | 39.8 | 28.5 | -0.1 | 2.176 |
| | 1B | 55.5 | 29.7 | 50.6 | 37.7 | 25.8 | 0.0 | 2.376 |
| | 1C | 33.9 | 3.8 | 30.4 | 36.9 | 30.1 | -0.2 | 2.234 |
| (111) | 1D | 60.2 | 39.6 | 55.2 | 29.3 | 20.7 | -0.3 | 2.318 |
| | 1E | 55.5 | 29.7 | 50.6 | 37.7 | 25.8 | 0.0 | 2.376 |
| | 1A 1B 1C 1D 1E | 38.4 | 14.4 | 34.2 | 25.5 | 24.0 | -0.5 | 2.363 |
| | 2A 1B 1C 1D 1E | 34.4 | 11.8 | 30.5 | 21.9 | 22.6 | *0.2* | 2.843* |

| | | | | | | | | |
|---|---|---|---|---|---|---|---|---|
| (021) | 1A | 67.3 | 43.3 | 62.4 | 32.8 | 24.0 | -0.5 | 2.343 |
| | 1B | 45.4 | 21.2 | 40.5 | 28.1 | 24.2 | -0.1 | 2.394 |
| | 1C | 34.4 | 16.5 | 30.3 | 23.4 | 17.9 | 0.0 | 2.392 |
| | 1A 1B | 56.5 | 33.5 | 51.7 | 29.6 | 23.1 | -0.3 | 2.378 |
| (110) | 1A | 30.0 | 13.8 | 25.4 | 29.1 | 16.2 | -0.1 | 2.370 |
| | 1B | 30.0 | 13.7 | 25.4 | 29.2 | 16.3 | -0.1 | 2.369 |
| | 1C | 26.4 | 4.4 | 20.9 | 27.5 | 22.0 | -0.1 | 2.330 |
| | 1D | 45.8 | 29.2 | 40.7 | 24.4 | 16.6 | -0.1 | 2.313 |
| | 1(A,B) | 29.8 | 13.6 | 25.2 | 29.2 | 16.2 | -0.1 | 2.370 |
| | 1A 1C 1D | 33.3 | 15.6 | 28.4 | 24.9 | 17.7 | *0.4* | 2.366 |
| Average | | 44 | 23 | 39 | 27 | 21 | –0.3 | 2.4 |
| Std. dev. | | 12 | 11 | 12 | 5 | 4 | 0.8 | 0.1 |
| Minimum | | 23.3 | 0.6 | 18.1 | 19.6 | 13.6 | -4.7 | 2.176 |
| Maximum | | 68.1 | 49.8 | 63.0 | 39.8 | 30.1 | 0.4 | 2.843 |

*: average only for molecules effectively adsorbed on Mg sites, see Figure 4.IV.

Data resumed in Table 3 confirmed the weak nature of CO adsorption on forsterite surfaces. Mg-C bond distance ranges from 2.176 ("(111) 1A" case) to 2.843 ("(111) 2A, 1B, 1C, 1D, 1E" case) Å, with $2.4 \pm 0.1$ Å resulting by averaging all values of the last column. The only outliner is for the "(111) 2A, 1B, 1C, 1D, 1E" case in which $\langle d_{Mg-C} \rangle = 2.843$ Å: it is worth noting that this is not due to the contribution of the extra CO molecule initially adsorbed on Mg A and lying flat on previously adsorbed CO molecules (Figure 4.IV).

By comparing related cases in Table 3, it is easy to compute the contribution to the binding energy for a specific single adsorption process. For example, the net BE of the "lying flat" CO molecule of the "(111) 2A, 1B, 1C, 1D, 1E" case can be computed as 6·BE [(111) 2A, 1B, 1C, 1D, 1E] – 5·BE [(111) 1A, 1B, 1C, 1D, 1E] giving a value of 14.4 kJ mol$^{-1}$. This value may be representative to understand the formation of a CO ice.

BE-disp values range from 23.3 ("(001) 2A, 2B" case) to 68.1 ("(101) 1A" case) kJ mol$^{-1}$, showing exclusively physisorption of CO on the forsterite surfaces.

BSSE and dispersion interactions play fundamental and opposite roles. The former affects the BE-disp values by 56% on average, a value close to that resulting from the adsorption of drugs on amorphous silica.[101] Dispersion contribution to the BE-disp is also large (50% on average of the BE-disp) and, unlike BSSE, is a physically related quantity. For the "(001) 2A, 2B" or the "(111) 1C" cases, they entirely dominate the interaction between CO and forsterite surfaces.

In the penultimate column of Table 3 we also report the CO lateral interactions $E_L$ simply computed as the energy differences between the B3LYP-D* energy of the corresponding periodic layers of adsorbed CO for each specific case with respect to the same number of isolated CO molecules (see the SI for the details). The sign convention is the same as for the BEs, *i.e.* negative values means repulsive interactions. All values, except the "(001) 2A, 2B" case, are very small and negligible with respect to BEs, showing that the BE for a specific site is not influenced by the CO adsorbed on a nearby site (site-site independence). The relatively high value of $E_L$ ($-4.7$ kJ mol$^{-1}$), for "(001) 2A, 2B" case is due to the repulsive interaction between the two CO molecules co-adsobed on the same Mg B site (compare with the "(001) 2A, 1B" (0.3 kJ mol$^{-1}$ case, see Figure S13).

We did not found any significant correlation between the binding energy, or the enthalpy variations, and the Mg-C distance.

We did not consider the adsorption of CO oxygen-down. This is known to occur, for instance, in acidic and cation exchanged zeolites[102,103] while it has never been observed for CO adsorption on extended ionic surfaces. To further check that this is the case also here, we computed the BE for the O-down adsorption for some cases, for instance, the "(120) 1C case": a value of 17.5 kJ mol$^{-1}$ resulted, to be contrasted with the C-down value of 35.5 kJ mol$^{-1}$. This large difference in BE ensure that the O-down population is entirely negligible at the temperature of interest and does not play a relevant role in the features of the forsterite/CO adsorption.

*3.3 CO desorption times*

Since the first observations of the ISM in the IR region were carried out, different astrophysical models for dust grains have been proposed.[7,104–110] Several parameters characterize the models, whose values derive either from direct observations (when possible) or from "terrestrial techniques", such as laboratory experiments and computer modelling. Examples are the residence times of adsorbed species (molecules, ices but also of layers of carbonaceous material[110]) on the surface of grains at a given temperature and pressure.

Along that line, the present computed data can be used to predict the desorption kinetics of CO from

forsterite grains through the Eyring equation for the kinetic desorption constant $k_D$.

Since CO adsorbs barrier less, as no chemical bond making/breaking occurs at the forsterite

surfaces, the Gibbs free activation energy of desorption $\Delta_{des}G^{\neq}$ coincides with the negative of the

Gibbs free energy of adsorption $\Delta_{des}G = -\Delta_{ads}G \equiv \Delta_{des}G^{\neq}$. However, in our case, $\Delta_{des}G$ values

coincide in turn with $\Delta_{des}A$ values computed according to Eq. 5 at a given temperature. With these

assumptions, desorption times $t_{des}$ from Eq. 6 are normalized to 10 Myr, assumed as the typical

lifetime of MCs.[111] Figure 5 shows the $\log(t_{des}/10 \text{ Myr})$ vs $T^{-1}$ trend in the 0÷100 K range for the

mono-most-bound case of each surface. At the low temperatures characterizing cooler clouds,

desorption times are much greater than the times typically required for MCs evolution (this

evolution times are represented by the straight lines in the inset box of Figure 5) and becomes

comparable only at temperature of about 75-100 K. For the complete data set, see Table S1.
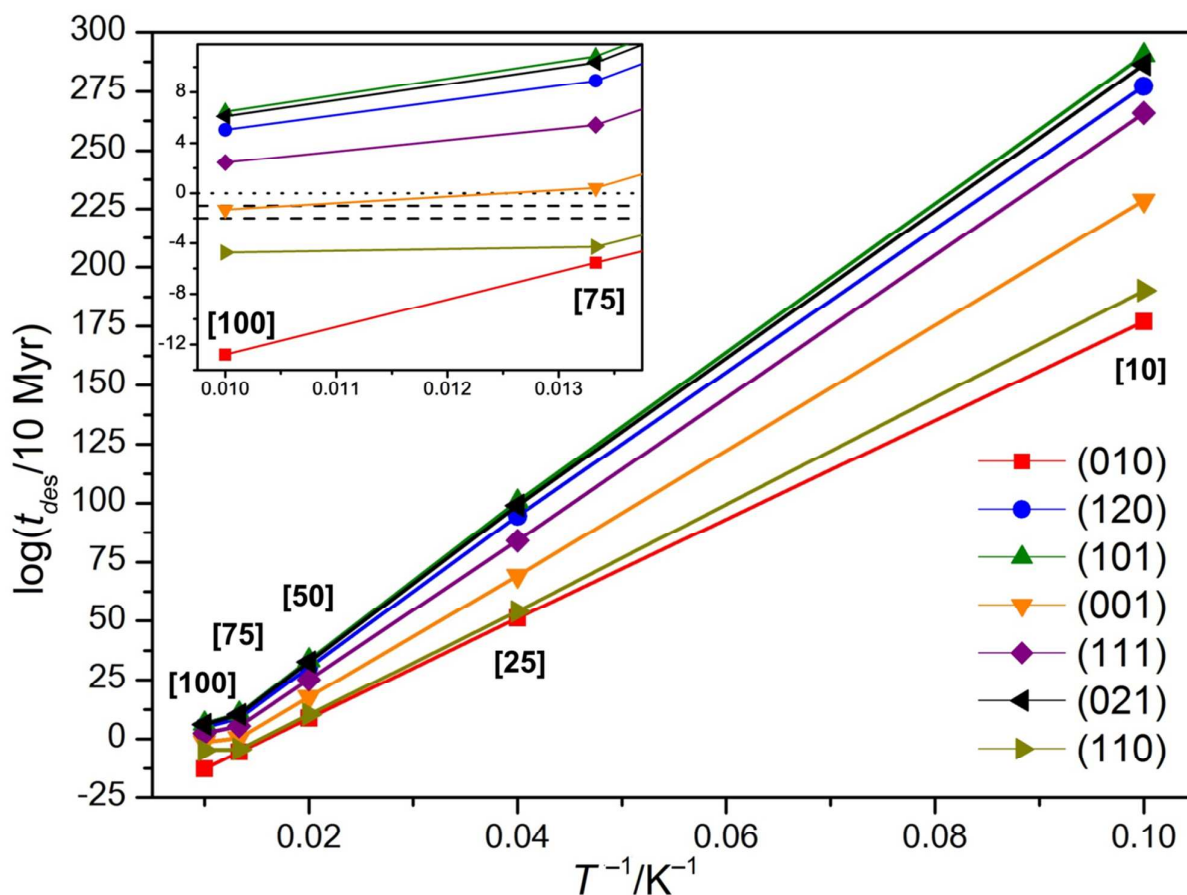
**Figure 5** CO desorption times ($t_{des}$) for the mono-most-bound cases of each surface as a function of temperature ($T$). Times are normalized with respect to 10 Myr – the typical lifetime of a MC – and reported in logarithmic scale for convenience. The values in square brackets represent the different temperatures to which desorption times have been computed according to Eq. 6. Straight lines in the inset box represent time intervals for the MCs evolution: gravitational collapse time ($10^5 \div 10^6$ yr, dashed lines)[111] and lifetime ($10^7$ yr, dotted line).[112–115]

A long residence time increases the probability of molecular encounters at the surfaces, more likely through the Eley-Rideal mechanisms, providing the base for the formation of COMs. At higher T, desorption/re-adsorption processes becomes feasible so that the Langmuir-Hinshelwood mechanism accounts for CO reactions. Clearly, the present data can be profitably used in models assuming the dynamical evolution of clouds.[109,110]

*3.4 Vibrational frequencies of CO molecules*

When dealing with adsorbed CO molecules, a key quantity is their stretching frequency shift values with respect to the free CO one. Positive, or hypsochromic, shifts are referred as "blue shift", while

negative, or bathochromic, ones as "red shift". Blue shift implies a CO bond shortening with a

corresponding increase in the bond force constant and vibrational frequency. The reverse happens

for red-shifted cases.[116] The relevance of the CO vibrational shift is to probe the electric field and

the chemical features of the adsorbing surface sites. In transitional metals with electronic

configuration different from $d^0$, the main contribution to the interaction energy for the metal-CO

system is due to the $\pi$-backdonation from $d$ orbitals of the metal to the antibonding $2\pi^*$ LUMO of

the CO. Thus, the anti-bonding levels of CO become more populated, weakening the C-O bond. On

the other hand, the $\sigma$-donation from the non-bonding $5\sigma$ HOMO produces a reinforcement of the C-

O bond although of minor entity.[93–95,116] For non-$d$/$d^0$ metals (as the case of $Mg^{2+}$), backdonation is

prevented so the only possible interaction is the $\sigma$-donation from the CO-HOMO to the metal $s$/$p$-

orbital. Due to the weak anti bonding nature of the $5\sigma$ HOMO, the C-O bond is reinforced and

vibrational blue shifts resulted. However, this "classical" point of view has been questioned since it

does not produce sufficiently high interactions energies and large blue shifts. Thus, it has been

suggested that a large part of the interaction between CO and non-$d$/$d^0$ metals would then be played

by pure electrostatic effects.[96,97,116] More specifically, the electric field originated by the metal

cation would produce a polarization of both $\sigma$ and $\pi$ CO bonding orbitals along the O → C direction,

enhancing the covalent character and the strength of the CO bond.[98]

For $d^{10}$ metals, back-donation is also expect to occur but in some cases, as in $Zn^{2+}$ zeolites, they

seem to behave like non-$d$/$d^0$ metals.[117]

For Ca(II), Na(I), Zn(II), Ag(I) and Cu(I) exchanged zeolites, Bolis and coworkers reported the

existence of a liner correlation between experimental $\Delta\bar{\nu}$ and the values of desorption enthalpies in

the CO zero coverage limit.[117,118] They showed that any deviation from the linear behavior reveals

the incoming effect due to increasing charge transfer and back-donation towards CO. Despite the

highly ionic nature of the forsterite surfaces, we did not observe a straight linear correlation

between the computed desorption enthalpies (or, equivalently the BEs) and the CO vibrational

shifts, but only a broad trend (data not shown). Furthermore, for some cases we computed red-

shifted values. These cases represent a small percentage of the total (7 negative shifts out of a total of 73, see Figure 6.II and Table S2). The missing expected linear correlation between energetic and spectroscopic features reveals a more complex interaction for the present case with respect to the systems considered by Bolis et al,[117,118] in which the surrounding of the adsorbing cation was much more regular than in forsterite surfaces. The complexity of the surface sites in the present case (*vide supra*) and the important role of dispersion interaction deviate from the simpler ion/dipole model for the systems accounted for by the Bolis et al.[117,118] Nevertheless, we have found a very good linear correlation between $\Delta \bar{v}$ shifts and C-O distances ($d_{CO}$), as predicted by the Blyholder model[116] (Figure 6.I). This linear relation is useful for quickly evaluating the CO vibrational shift without performing an expensive frequency calculation, by only using its CO bond length.

To the best of our knowledge, while bathochromic shifts have been reported for CO adsorbed in cation-exchanged zeolites,[102,103] no experimental evidence of that has ever been reported for CO adsorbed on extended ionic surfaces in the CO low coverage regime. For the zeolite case, the CO bathochromic shifts were proved to be due to CO adsorbed oxygen-down at the cations, which is in thermodynamic equilibrium with the most stable C-down isomer, even if with a much reduced population (*vide supra*).

In our set, the "(111) 2A, 1B, 1C, 1D" case ($\Delta \bar{v}$ = –2 cm$^{-1}$) may be rationalized because of the high CO coverage, in which the second CO molecule initially adsorbed on Mg A lies in a configuration almost flat without evidence of C-Mg interaction (Figure 4.IV).

Four out of the six remaining bathochromic shifts belong to cases of multi-loading CO coverage, in which lateral interactions among adsorbed CO molecules may cause negative CO frequency shifts through in space coupling. The remaining two cases, "(101) 1B" and "(110) 1C", are CO mono-loading ones, in which the dominant quadrupolar nature of CO comes into play to account for the bathochromic shifted values.
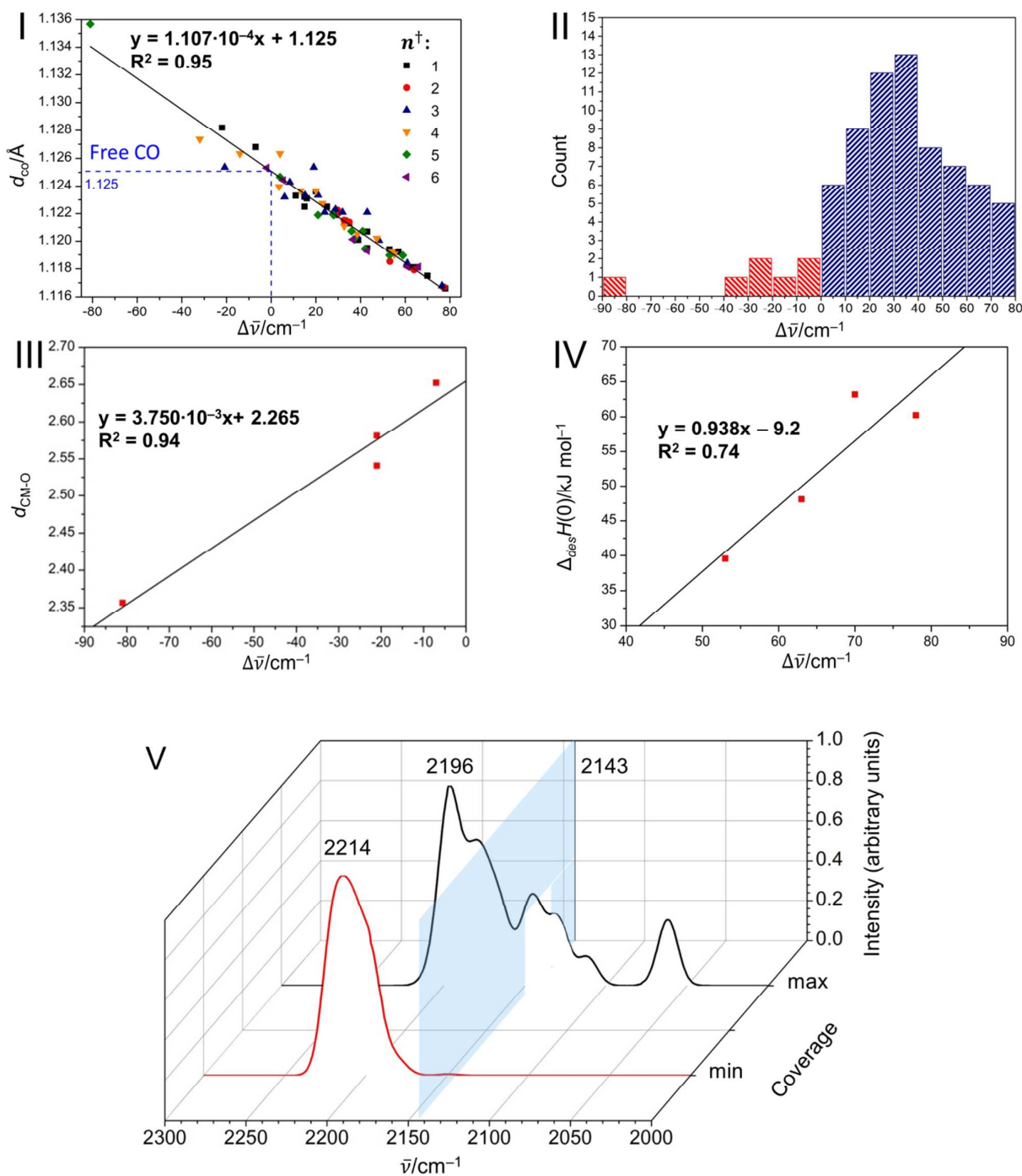
**Figure 6.** I. Linear correlation between CO bond lengths and $\Delta\bar{v}$ values. $n^{\dagger}$, number of CO molecules *per* unit cell. II. Histogram distribution of $\Delta\bar{v}$ values. III. Negative $\Delta\bar{v}$ *vs* the distance between the center of mass of CO molecules and the closest O atom of the SiO$_4$ moiety. IV. CO $\Delta\bar{v}$ values *vs* desorption enthalpy (at 0 K, Eq. 4) for the most bound cases of the four most representative surfaces (see MRI of Table 2). V. Overall simulated infrared spectra in the CO stretching region at 100 K at lowest (min) and highest (max) CO coverage. Light-blue plan: free CO reference frequency (2143 cm$^{-1}$).

As pointed out by the structures reported in Figures 3.II and 3.III (but also in Figures S2-S8 of the SI), forsterite surfaces are really complex from an electrostatic point of view. Therefore, the interaction between CO and exposed Mg sites cannot be interpreted through a simple dipole-charge model, as interactions involving the negative O atoms of the exposed $SiO_4$ units with the positive belt of the CO quadrupole may play a fundamental role.

*3.5 Interplay between electrostatic and dispersive interactions*

Interplay between electrostatic and dispersion interactions, evaluated by the Grimme's correction, may affect the final structures in several ways. To elucidate the role of both aspects, we re-optimized at B3LYP level (no dispersion included): i) all the most bound cases for all the seven surfaces; ii) the two mono-coverage cases affected by red-shifted frequencies, "(101) 1B" and "(110) 1C", respectively. For the sake of brevity, we show results referring only to two representative cases, the "(010) 1A" and the "(101) 1B" (Figure 7). All the other tested cases are available in the SI.
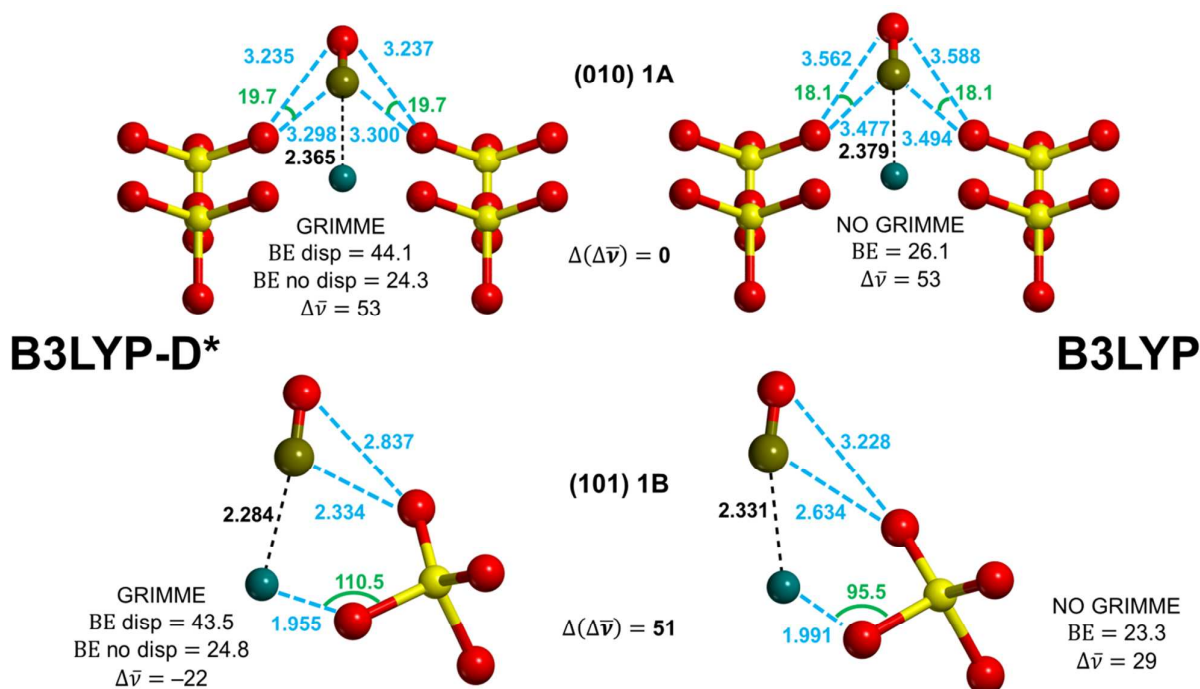
**Figure 7.** Optimized structures with (left) and without (right) Grimme's correction for two representative cases. Distances in Å, energies in kJ mol$^{-1}$ and CO frequency shifts in cm$^{-1}$.

As expected, at B3LYP level, all the distances increase with respect to B3LYP-D* case, due to the missing attractive term. For the "(010) 1A" case (and similarly related ones, see SI), due to the symmetry constraints forcing CO to stay aligned on top of Mg ion (Figure 7, top), no difference in the CO frequency shifts resulted, despite the general shrinking of the intermolecular distances. When moving to the "(101) 1B" case, the differences between the two geometries are more subtle: dispersion is dramatically enlarging the value of the surface Mg···O-Si angle which, in turn, affects the way in which CO becomes adsorbed. Comparison of the optimized B3LYP with the corresponding B3LYP-D* structure (see structures at the bottom of Figure 7) shows how dispersion brings CO closer to the negatively charged oxygen atom belonging to the most exposed SiO$_4$ tetrahedron. This interaction is attractive, when considering the quadrupolar electrostatic nature of the CO molecule (see Figure 3.I). Nevertheless, the mechanism behind the charge flux rearrangement of CO for this case is such that a bathochromic shift of the CO stretching frequency occurs. Interestingly, Figure 6.III shows a trend between the negative shift $\Delta\bar{v}$ values and the distances between the centers of mass of CO molecules and the closest oxygen atom of a SiO$_4$ unit.

This relation hold true for – "(101) 1B", "(101) 1A, 1B, 1C", "(101) 1A, 1B, 1C, 1D, 1E" and "(110) 1C" – cases, in which a single bathochromic shift occurs for a single CO molecule (see Table S2 of the SI). For the "(001) 2A, 2B" cases, where three CO molecules are involved in two modes characterized by bathochromic shifts, the distance between the CO center of mass and the closest oxygen atom of the $SiO_4$ moiety cannot be worked out. As the number of cases is very limited, we do not claim a statistical robustness for the graph in Figure 6.III. Nevertheless, we believe it contains a physically sensible message, *i.e.* "the shorter the distance between the centers of mass of CO to the nearby surface oxygen, the larger is the bathochromic shift suffered by CO".

This complex behavior is probably the reason why the whole set of energetic data and vibrational ones do not rest on a linear correlation, as found through experiments by Bolis *et al.*[117] for CO adsorbed in cation-exchanged zeolites. Nevertheless, Figure 6.IV, shows that, for the most bound cases of the most representative surfaces, a good correlation holds true.

Figure 6.V summarizes the overall simulated IR spectra in the CO stretching region corresponding to the lowest/highest CO coverage. Experimentally, the most interesting case is for the zero-limit CO coverage,[117] which correspond to the "min" spectrum. Each spectrum results by a linear weighted sum of the CO stretching frequency value for all considered cases within the "min/max" coverage regimes. The weights of the sum are the Boltzmann's factor $\exp(-\Delta(BE)/RT)$ computed at $T = 100$ K using the difference $\Delta(BE)$ in CO relative binding energy. MRI values of Table 2 also multiply each weight, to account for the spatial extension of each surface. The adopted temperature is close to that of liquid nitrogen to mimic most experimental conditions. The spectrum corresponding to the "min" coverage only shows components higher than 2143 cm$^{-1}$ (free CO), in line with the expected hypsochromic shift observed from the vast majority of experiments dealing with CO on extended oxide surfaces. The main contribution to this spectrum derives from the CO mono-most-bound cases for each surface. At maximum coverage ("max"), the spectrum suffers a shift toward lower wave numbers, due to the bathochromic contributions to the CO frequency

deriving from multi-loading cases (*vide supra*) for which both BE and $\Delta\bar{\nu}$ values are lower with respect the mono loading cases.

*3.6 Thermodynamic analysis*
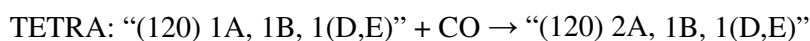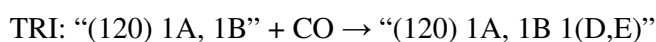
For each of the 37 considered cases, we computed the surface free energies $G_S(T, P, \sigma)$ and the related adsorption free energies $\Delta_{ads}G(T, P, n)$ according to Eq. 7 and 8, at the pressure value of $10^{-16}$ Pa which is indicative of the physical conditions characterizing MCs.[74] The stability diagrams ($G_S$ *vs* $T$ trend) are shown in the top-left part of Figure 8 for all CO adsorption cases of the (120) surface. The diagrams show the thermodynamically favored structures for which $G_S < E_S$ at a given temperature. Since the adsorption is a true physisorption (*vide supra*), the most stable structures (at a given $T$) are the ones expected to exists; therefore these diagrams can be interpreted also as phase diagrams. For the sake of brevity, we do not show data referring to all the other surfaces as their calculation is straightforward.

As you can see from the left of Figure 8, the case of highest CO coverage, "(120) 2A 1B 1(D,E)", is the most stable up to 50 K, since it has the lowest values of $G_S$. Beyond this point, there is a crossing (green-dashed line) for the adsorption of two CO per unit cell, "(120) 1A 1C", which is the most stable one only up to about 60 K. Over 60 K, the mono CO covered "(120) 1A" case, the most bound one at 0 K and 0 Pa (see Table 3), becomes the most stable one.
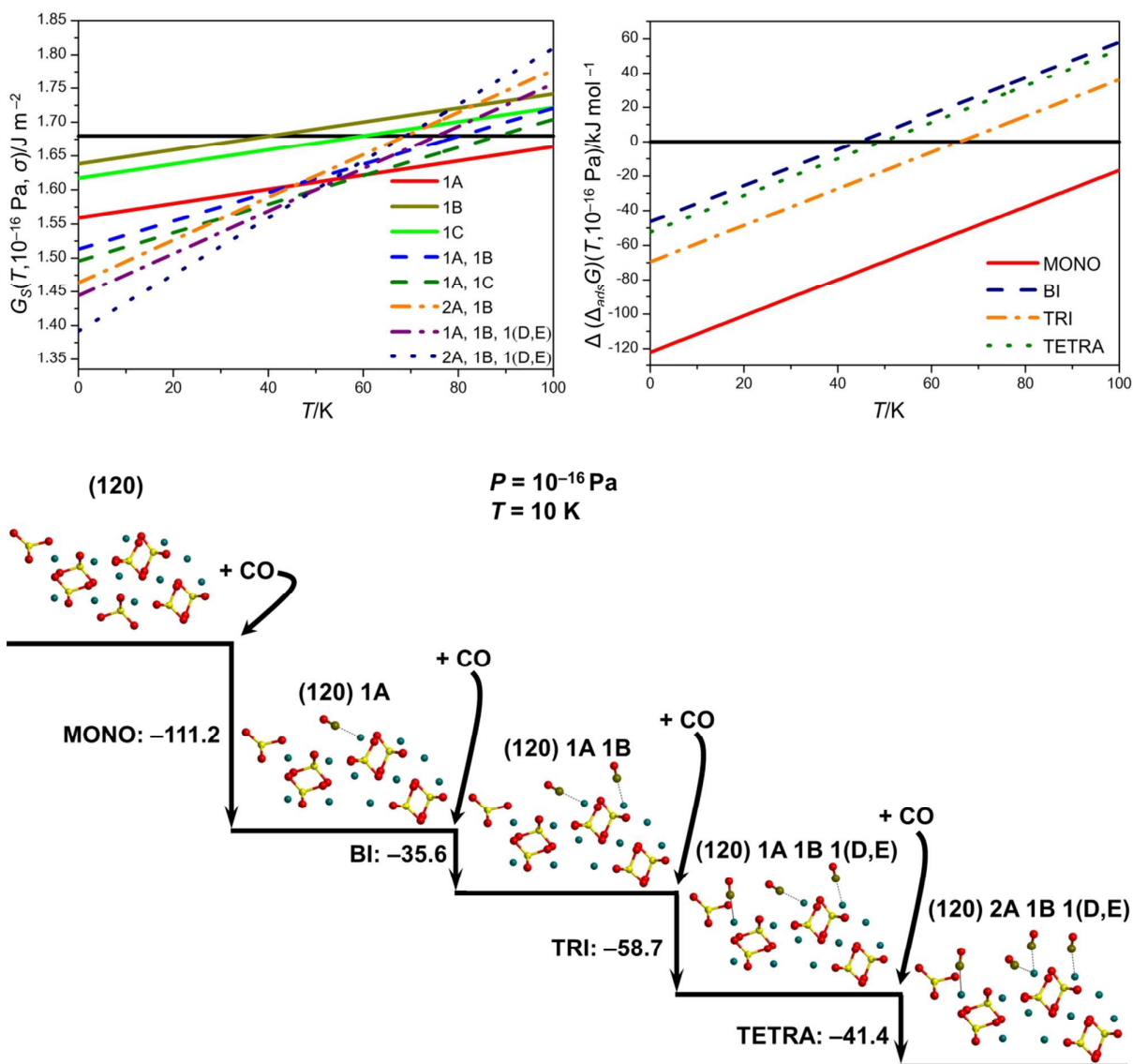
**Figure 8.** Top-left: stability diagrams for all CO adsorbed cases of the (120) surface. Pressure is equal to $10^{-16}$ Pa. Horizontal black line corresponds to the $G_S = E_S$ condition. Different CO coverages as lines: solid ($n^{\dagger} = 1$), dashed ($n^{\dagger} = 2$), dot-dashed ($n^{\dagger} = 3$), short-dotted ($n^{\dagger} = 4$). Top-right: variations of adsorption Gibbs free energy for some single-adsorption processes occurring at the (120) surface (see text) as a function of temperature. Pressure is equal to $10^{-16}$ Pa. Different processes as lines: (120) + CO → "(120) 1A" (solid, MONO), CO + "(120) 1A" → "(120) 1A 1B" (dashed, BI), CO + "(120) 1A 1B" → "(120) 1A 1B 1(D,E)" (dot-dashed, TRI), CO + "(120) 1A 1B 1(D,E)" → "(120) 2A 1B 1(D,E)" (short-dotted, TETRA). Bottom: schematic representation of all Gibbs free energy variations involved in the formation of the most-covered case for the (120) surface, the "(120) 2A, 1B, 1C" one (at $10^{-16}$ Pa and 10 K) as a sequence of single-adsorption processes. Numbers beside vertical lines represent the variations of adsorption Gibbs free energy for each step in kJ mol$^{-1}$. For all the involved structures, we show a detail of the side views (see also Figure S10 and S11).

Exploiting Eq. 8 we also computed the adsorption Gibbs free energies $\Delta_{ads}G(T,P,n)$ for each of the 37 simulated cases at $10^{-16}$ Pa. However, again we show only data referring to the (120) surface. Top-right corner of Figure 8 reports the variations in adsorption Gibbs free energies for some single CO molecule adsorption processes, *i.e.* $\Delta(\Delta_{ads}G) = \Delta_{ads}G(T,P,n+1) - \Delta_{ads}G(T,P,n)$ as a function of temperature. For the sake of clarity, we report only those processes involved in the formation of the most covered case, the "(120) 2A, 1B, 1(D,E)" one (for a more complete picture, see Figure S26). For the whole $G_S(T,P,\sigma)$ and $\Delta_{ads}G(T,P,n)$ data set, see Table S3). Specifically, the considered processes are:

MONO: (120) + CO → "(120) 1A"

BI: "(120) 1A" + CO → "(120) 1A, 1B"

TRI: "(120) 1A, 1B" + CO → "(120) 1A, 1B 1(D,E)"

TETRA: "(120) 1A, 1B, 1(D,E)" + CO → "(120) 2A, 1B, 1(D,E)"

Selecting one temperature, the total Gibbs free energy of adsorption for the step-by-step formation of the "(120) 2A, 1B, 1(D,E)" case can be easily computed. For example, in the bottom part of Figure 8, we report all the energetics steps at 10 K. At this low $T$ (and $P$) all formation steps are thermodynamic favored. At temperatures higher than 65 K only the MONO process (formation of the mono-covered case) is thermodynamic favored.

However, we would like to stress that thermodynamic arguments are based on the assumption of equilibrium between gas and solid phase[79,80] (see SI - Computational details - *Surface free energies and adsorption free energies (Eq. 7 and 8)*) which may not be easily fulfilled in the harsh physical conditions of the ISM, despite the very long lifetimes of MCs.

**Conclusions**

We investigated at a B3LYP-D*[49–51,59] level of theory (inclusive of dispersion contribution to the interaction energy) the adsorption of carbon monoxide (CO) on seven different surfaces of forsterite ($Mg_2SiO_4$), the Mg end-member of olivines, one of the main component of the interstellar core dust

grains in Molecular Clouds (MCs).[2,119–121] CO is the second most abundant gas-phase molecular

species discovered in MCs, after $H_2$.[2] For these reasons, elucidating the details of the CO interaction

may be important from an astrochemical point of view. We focused on the (001), (010), (101),

(110), (111), (120) and (021) surfaces within the slab approach, following the work of Bruno *et al.*

adopting the same extended Gaussian basis set.[45,46] For the seven surfaces we provide: i) the

optimized structures; ii) the surface energies; iii) the Wulff's polyhedron; iv) the electrostatic

potential maps. The most relevant conclusion from structural and electrostatic features is that

forsterite surfaces have complex morphologies, which do not allow to adopt the simple charge-

dipole model to elucidate the CO/surface interactions.[116,117] That simplified model was commonly

used in the literature, to interpret the experiments and simulation for CO adsorbed on regular oxide

surfaces (NaCl, MgO, etc.) or in cation-exchanged zeolites. We revealed the role of the large CO

quadrupole moment coupled with the subtle geometrical changes in the surface structure induced by

the dispersion components of the energy to rationalize both energetic of adsorption and CO

stretching frequency variations with respect to free CO. We found that CO only physisorbs (no

bond making/breaking with the forsterite surface atoms) on exposed Mg cations of surface

forsterite, with desorption enthalpy variations at 0 K per CO molecule in the 18-63 kJ mol$^{-1}$ range,

depending on the surface and CO coverage. We revealed that dispersion interaction plays a

fundamental role, accounting, as average, for the 50% of the total energy of interaction. Lateral

interaction between adsorbed CO is also negligible. For all the optimized structures, we have

computed the CO stretching frequencies and the related IR spectra. We did not find a robust linear

correlation between CO interaction energy and the corresponding CO frequency shift with respect

to the gas phase, as usually reported for CO adsorbed in simpler oxides or cation-exchanged

zeolites, in the zero-coverage limit.[117] We discovered that dispersion interactions have a key role in

deforming the surface local environment on which the adsorbed CO molecule resides for some of

the considered surfaces. This, in turn, has a dramatic effect on the CO frequency shift with respect

to the gas-phase molecule, due to subtle interaction between the CO quadrupole moment and the

negative oxygen belonging to the nearest surface $SiO_4$ moiety. For these reasons, we computed 7

different adsorption cases, up to a total of 73, in which bathochromic CO frequency shifts occur. Of

these seven negative shifts, five refer to multi-loading cases (four to maximum coverage cases),

thus lateral repulsion between adsorbed molecules may explain these negative shifts, and only two

to mono-covered cases. Although we did not observe a correlation between adsorption energy and

CO frequency shifts for the above reasons, we found a good linear relation between the CO bond

lengths and the corresponding frequency shifts: this may serve to guess the CO frequency from its

geometry only, without resorting to the expensive frequency calculations. We simulated the overall

IR spectrum of the adsorbed CO as a function of CO coverage, which may be useful to interpret

experimental data coming from both the laboratory and from deep space observations. The

thermodynamic treatment of CO adsorption, which assumes equilibrium between the gas and solid

phases, gives information about the most stable adsorbed phase as a function of $T$ at a given $P$ and

the considered surface, allowing to disentangle the component of the heat of adsorption in

temperature programmed desorption and microcalorimetric experiments. However, our

thermodynamic treatment is based on the assumption that an equilibrium between gas and solid

phase is always established even in the harsh conditions characterizing MCs, an assumption that

may not be operative. The present work is also relevant in for astrochemical modelling purposes, in

which kinetics of CO desorption may be computed using the accurate values provided by the

Quantum-Mechanical calculations. Thus, we simulate desorption times exploiting our computed

energetic features. They can be incorporated on such models accounting for dynamical evolution of

interstellar objects.[109,110] One limitation of this work is the adoption of perfect periodic forsterite

surfaces to model the core dust grains. We outline again that, although silicates in interstellar clouds

are expected to be highly amorphous (5% of crystallinity), other regions such as protostellar and

circumstellar disks and the interplanetary medium should be characterized by higher percentages of

crystalline silicates.[7,8] Thus, our perfectly crystalline models could well represent what happens in

these regions which dynamically derive from the evolution of proper clouds. In our laboratory, we

are already simulating nano-sized forsterite grains, therefore closer to the real grain sizes. It will be challenging to compare CO adsorption feature of the extended surfaces with that resulting on the nano-clusters in which the amorphous nature is more pronounced than the crystalline surfaces.

**Acknowledgments**

**Supporting Information**

Computational details: basis set, DFT grid, threshold parameters, optimizations and frequency calculations details, derivations of binding energies, desorption enthalpies and (surface) free energies, bulk and slab features (Figures S1-S8), energetic features of CO adsorption on slabs (Figures S9-S16), kinetic analysis for CO desorption (Table S1), IR vibrational analysis for adsorbed CO (Table S2), role of dispersive interaction in some cases (Figures S17-S25), thermodynamic analysis (Table S3, Figure S26).

**Authors Information**

Corresponding author

Email: piero.ugliengo@unito.it

ORCID

Lorenzo Zamirri: 0000-0003-0219-6150

Marta Corno: 0000-0001-7248-2705

Albert Rimola: 0000-0002-9637-4554

Piero Ugliengo: 0000-0001-8886-9832

**References**

(1)   Endres, C. P.; Schlemmer, S.; Schilke, P.; Stutzki, J.; Müller, H. S. P. The Cologne Database for Molecular Spectroscopy, CDMS, in the Virtual Atomic and Molecular Data Centre, VAMDC. *J. Mol. Spectrosc.* **2016**, *327*, 95–104.

(2)   Ehrenfreund, P.; Charnley, S. B. Organic Molecules in the Interstellar Medium, Comets, and Meteorites: A Voyage from Dark Clouds to the Early Earth. *Annu. Rev. Astron. Astrophys.* **2000**, *38*, 427–483.

(3)   Herbst, E.; van Dishoeck, E. F. Complex Organic Interstellar Molecules. *Annu. Rev. Astron. Astrophys.* **2009**, *47*, 427–480.

(4)   Zook, H. A. Spacecraft Measurements of the Cosmic Dust Flux. In *Accretion of Extraterrestrial Matter Throughout Earth's History*; Peucker-Ehrenbrink, B., Schmitz, B., Eds.; Springer US: New York, 2001; pp 75–92.

(5)   Belloche, A.; Menten, K. M.; Comito, C.; Müller, H. S. P.; Schilke, P.; Ott, J.; Thorwirth, S.; Hieret, C. Detection of Amino Acetonitrile in Sgr B2(N). *Astron. Astrophys.* **2008**, *492*, 769–773.

(6)   Henning, T. Cosmic Silicates. *Annu. Rev. Astron. Astrophys.* **2010**, *48*, 21–46.

(7)   Li, A.; Draine, B. T. On Ultrasmall Silicate Grains in the Diffuse Interstellar Medium. *Astrophys. J.* **2001**, *550*, L213–L217.

(8)   Molster, F. J.; Yamamura, I.; Waters, L. B. F. M.; Tielens, A. G. G. M.; de Graauw, T.; de Jong, T.; de Koter, A.; Malfait, K.; van den Ancker, M. E.; van Winckel, H.; et al. Low-Temperature Crystallization of Silicate Dust in Circumstellar Disks. *Nature* **1999**, *401*, 563–565.

(9)   Boogert, A.; Gerakines, P.; Whittet, D. Observations of the Icy Universe. *Astron. Astrophys.* **2015**, *53*, 541–581.

(10)  Ehrenfreund, P.; Schutte, W. A. Infrared Observations of Interstellar Ices. In *Astrochemistry: from Molecular Clouds to Planetary Systems*; Minh, Y. C., van Dishoeck, E. F., Eds.; IAU

Symp. 197, ASP, 2000; pp 135–146.

(11)   Allamandola, L. J.; Bernstein, M. A. X. P.; Sandford, S. a; Walker, R. L. Evolution of Interstellar Ices. *Space Sci. Rev.* **1999**, *90*, 219–232.

(12)   Vasyunin, A. I.; Caselli, P.; Dulieu, F.; Jiménez-Serra, I. Formation of Complex Molecules in Prestellar Cores: A Multilayer Approach. *Astrophys. J.* **2017**, *842*, 33.

(13)   Navarro-Ruiz, J.; Sodupe, M.; Ugliengo, P.; Rimola, A. Interstellar H Adsorption and $H_2$ Formation on the Crystalline (010) Forsterite Surface: A B3LYP-D2* Periodic Study. *Phys. Chem. Chem. Phys.* **2014**, *16*, 17447.

(14)   Collings, M. P.; Frankland, V. L.; Lasne, J.; Marchione, D.; Rosu-Finsen, A.; McCoustra, M. R. S. Probing Model Interstellar Grain Surfaces with Small Molecules. *Mon. Not. R. Astron. Soc.* **2015**, *449*, 1826–1833.

(15)   He, J.; Jing, D.; Vidali, G. Atomic Oxygen Diffusion on and Desorption from Amorphous Silicate Surfaces. *Phys. Chem. Chem. Phys.* **2014**, *16*, 3493–3500.

(16)   Collings, M. P.; Dever, J. W.; McCoustra, M. R. S. The Interaction of Carbon Monoxide with Model Astrophysical Surfaces. *Phys. Chem. Chem. Phys.* **2014**, *16*, 3479–3492.

(17)   Collings, M. P.; Anderson, M. a.; Chen, R.; Dever, J. W.; Viti, S.; Williams, D. A.; McCoustra, M. R. S. A Laboratory Survey of the Thermal Desorption of Astrophysically Relevant Molecules. *Mon. Not. R. Astron. Soc.* **2004**, *354*, 1133–1140.

(18)   Bertin, M.; Fayolle, E. C.; Romanzin, C.; Öberg, K. I.; Michaut, X.; Moudens, A.; Philippe, L.; Jeseck, P.; Linnartz, H.; Fillion, J.-H. UV Photodesorption of Interstellar CO Ice Analogues: From Subsurface Excitation to Surface Desorption. *Phys. Chem. Chem. Phys.* **2012**, *14*, 9929–9935.

(19)   Scott Smith, R.; Li, Z.; Dohna, Z.; Kay, B. D. Adsorption, Desorption, and Displacement Kinetics of $H_2O$ and $CO_2$ on Forsterite, $Mg_2SiO_4$ (011). *J. Phys. Chem. C* **2014**, *118*, 29091–29100.

(20)   Moore, M. H.; Ferrante, R. F.; Hudson, R. L.; Stone, J. N. Ammonia–Water Ice Laboratory

Studies Relevant to Outer Solar System Surfaces. *Icarus* **2007**, *190*, 260–273.

(21) Noble, J. A.; Congiu, E.; Dulieu, F.; Fraser, H. J. Thermal Desorption Characteristics of CO, $O_2$ and $CO_2$ on Non-Porous Water, Crystalline Water and Silicate Surfaces at Submonolayer and Multilayer Coverages. *Mon. Not. R. Astron. Soc.* **2012**, *421*, 768–779.

(22) Thrower, J. D.; Collings, M. P.; Rutten, F. J. M.; McCoustra, M. R. S. Laboratory Investigations of the Interaction between Benzene and Bare Silicate Grain Surfaces. *Mon. Not. R. Astron. Soc.* **2009**, *394*, 1510–1518.

(23) Vidali, G.; Roser, J. E.; Manicò, G.; Pirronello, V. Experimental Study of the Formation of Molecular Hydrogen and Carbon Dioxide on Dust Grain Analogues. *Adv. Space Res.* **2004**, *33*, 6–13.

(24) Escamilla-Roa, E.; Sainz-Díaz, C. I. Amorphous Ammonia-Water Ice Deposited onto Silicate Grain: Effect on Growth of Mantles Ice on Interstellar and Interplanetary Dust. *J. Phys. Chem. C* **2014**, *118*, 3554–3563.

(25) Kerisit, S.; Bylaska, E. J.; Felmy, A. R. Water and Carbon Dioxide Adsorption at Olivine Surfaces. *Chem. Geol.* **2013**, *359*, 81–89.

(26) Goumans, T. P. M.; Richard, C.; Catlow, C. R. A.; Brown, W. A. Formation of $H_2$ on an Olivine Surface: A Computational Study. *Mon. Not. R. Astron. Soc.* **2009**, *393*, 1403–1407.

(27) Goumans, T. P. M.; Bromley, S. T. Hydrogen and Oxygen Adsorption on a Nanosilicate - A Quantum Chemical Study. *Mon. Not. R. Astron. Soc.* **2011**, *414*, 1285–1291.

(28) Garcia-Gil, S.; Teillet-Billy, D.; Rougeau, N.; Sidis, V. H Atom Adsorption on a Silicate Surface: The (010) Surface of Forsterite. *J. Phys. Chem. C* **2013**, *117*, 12612–12621.

(29) Kerkeni, B.; Bromley, S. T. Competing mechanisms of Catalytic $H_2$ Formation and Dissociation on Ultrasmall Silicate Nanocluster Dust Grains. *Mon. Not. R. Astron. Soc.* **2013**, *435*, 1486–1492.

(30) Downing, C. A.; Ahmady, B.; Catlow, C. R. A.; de Leeuw, N. H. The Interaction of Hydrogen with the {010} Surfaces of Mg and Fe Olivine as Models for Interstellar Dust

Grains: A Density Functional Theory Study. *Philos. Trans. R. Soc., A* **2013**, *371*, 20110592.

(31)  Navarro-Ruiz, J.; Ugliengo, P.; Sodupe, M.; Rimola, A. Does $Fe^{2+}$ in Olivine-Based Interstellar Grains Play Any Role in the Formation of $H_2$? Atomistic Insights from DFT Periodic Simulations. *Chem. Commun.* **2016**, *52* (42), 6873–6876.

(32)  de Leeuw, N. H.; Parker, S. C.; Catlow, C. R. A. Modelling the Effect of Water on the Surface Structure and Stability of Forsterite. *Phys. Chem. Miner.* **2000**, *27*, 332–341.

(33)  de Leeuw, N. H. Density Functional Theory Calculations of Hydrogen-Containing Defects in Forsterite , Periclase , and α-Quartz. *J. Phys. Chem. B* **2001**, *105*, 9747–9754.

(34)  Stimpfl, M.; Walker, A. M.; Drake, M. J.; de Leeuw, N. H.; Deymier, P. A. An Ångström-Sized Window on the Origin of Water in the Inner Solar System: Atomistic Simulation of Adsorption of Water on Olivine. *J. Cryst. Growth* **2006**, *294*, 83–95.

(35)  Muralidharan, K.; Deymier, P. A.; Stimpfl, M.; de Leeuw, N. H.; Drake, M. J. Origin of Water in the inner Solar System: A kinetic Monte Carlo Study of Water Adsorption on Forsterite. *Icarus* **2008**, *198*, 400–407.

(36)  King, H. E.; Stimpfl, M.; Deymier, P. A.; Drake, M. J.; Catlow, C. R. A.; Putnis, A.; de Leeuw, N. H. Computer Simulations of Water Interactions with Low-Coordinated Forsterite Surface Sites: Implications for the Origin of Water in the Inner Solar System. *Earth Planet. Sci. Lett.* **2010**, *300*, 11–18.

(37)  de Leeuw, N. H.; Catlow, C. R. A.; King, H. E.; Putnis, A.; Muralidharan, K.; Deymier, P. A.; Drake, M. J. Where on Earth has our Water Come From? *Chem. Commun.* **2010**, *46*, 8923–8925.

(38)  Prigiobbe, V.; Negreira, A. S.; Wilcox, J. Interaction between Olivine and Water Based on Density Functional Theory Calculations. *J. Phys. Chem. C* **2013**, *117*, 21203–21216.

(39)  Asaduzzaman, A.; Laref, S.; Deymier, P. A.; Runge, K.; Cheng, H.-P.; Muralidharan, K.; Drake, M. J.; Deymier, P. A. A First-Principles Characterization of Water Adsorption on Forsterite Grains. *Philos. Trans. R. Soc., A* **2013**, *371*, 20110582–20110582.

(40) Goumans, T. P. M.; Catlow, C. R. A.; Brown, W. A.; Kastnerzb, J.; Sherwoodb, P. An Embedded Cluster Study of the Formation of Water on Interstellar Dust Grains. *Phys. Chem. Chem. Phys.* **2009**, *11*, 5431–5436.

(41) Watson, G. W.; Kelsey, E. T.; de Leeuw, N. H.; Harris, D. J.; Parker, S. C. Atomistic Simulation of Dislocations, Surfaces and Interfaces in MgO. *J. Chem. Soc. Faraday Trans.* **1996**, *92*, 433–438.

(42) Walker, A. M.; Woodley, S. M.; Slater, B.; Wright, K. A Computational Study of Magnesium Point Defects and Diffusion in Forsterite. *Phys. Earth Planet. Inter.* **2009**, *172*, 20–27.

(43) Ottonello, G.; Civalleri, B.; Ganguly, J.; Vetuschi Zuccolini, M.; Noël, Y. Thermophysical Properties of the α-β-γ Polymorphs of $Mg_2SiO_4$: A Computational Study. *Phys. Chem. Miner.* **2009**, *36*, 87–106.

(44) Navarro-Ruiz, J.; Ugliengo, P.; Rimola, A.; Sodupe, M. B3LYP Periodic Study of the Physicochemical Properties of the Nonpolar (010) Mg-Pure and Fe-Containing Olivine Surfaces. *J. Phys. Chem. A* **2014**, *118*, 5866–5875.

(45) Bruno, M.; Massaro, F. R.; Prencipe, M.; Demichelis, R.; De La Pierre, M.; Nestola, F. Ab Initio Calculations of the Main Crystal Surfaces of Forsterite ($Mg_2SiO_4$): A Preliminary Study to Understand the Nature of Geochemical Processes at the Olivine Interface. *J. Phys. Chem. C* **2014**, *118*, 2498–2506.

(46) Demichelis, R.; Bruno, M.; Massaro, F. R.; Prencipe, M.; De La Pierre, M.; Nestola, F. First-Principle Modelling of Forsterite Surface Properties: Accuracy of Methods and Basis Sets. *J. Comput. Chem.* **2015**, *36*, 1439–1445.

(47) Goumans, T. P. M.; Bromley, S. T. Efficient Nucleation of Stardust Silicates via Heteromolecular Homogeneous Condensation. *Mon. Not. R. Astron. Soc.* **2012**, *420*, 3344–3349.

(48) Dovesi, R.; Saunders, V. R.; Roetti, C.; Orlando, R.; Pascale, F.; Civalleri, B.; Doll, K.;

Harrison, N. M.; Bush, I. J.; D'Arco, P.; et al. Crystal14. User's Manual. Università di Torino, Torino 2014.

(49)   Becke, A. D. Density-Functional Exchange-Energy Approximation with Correct Asymptotic Behavior. *Phys. Rev. A* **1988**, *38*, 3098–3100.

(50)   Becke, A. D. A New Mixing of Hartree-Fock and Local-Density-Functional Theories. *J. Chem. Phys.* **1993**, *98*, 1372–1377.

(51)   Lee, C.; Yang, W.; Parr, R. G. Development of the Colle-Salvetti Correlation-Energy Formula into a Functional of the Electron Density. *Phys. Rev. B* **1988**, *37*, 785–789.

(52)   Noël, Y.; De La Pierre, M.; Maschio, L.; Rérat, M.; Zicovich-Wilson, C. M.; Dovesi, R. Electronic Structure, Dielectric Properties and Infrared Vibrational Spectrum of Fayalite: An Ab Initio Simulation with an All-Electron Gaussian Basis Set and the B3LYP Functional. *Int. J. Quantum Chem.* **2012**, *112*, 2098–2108.

(53)   De La Pierre, M.; Orlando, R.; Maschio, L.; Doll, K.; Ugliengo, P.; Dovesi, R. Performance of Six Functionals (LDA, PBE, PBESOL, B3LYP, PBE0, and WC1LYP) in the Simulation of Vibrational and Dielectric Properties of Crystalline Compounds. The Case of Forsterite $Mg_2SiO_4$. *J. Comput. Chem.* **2011**, *32*, 1775–1784.

(54)   Demichelis, R.; Civalleri, B.; Ferrabone, M.; Dovesi, R. On the Performance of Eleven DFT Functionals in the Description of the Vibrational Properties of Aluminosilicates. *Int. J. Quantum Chem.* **2010**, *110*, 406–415.

(55)   Noël, Y.; Catti, M.; D'Arco, P.; Dovesi, R. The Vibrational Frequencies of Forsterite $Mg_2SiO_4$: An All-Electron Ab Initio Study with the CRYSTAL Code. *Phys. Chem. Miner.* **2006**, *33*, 383–393.

(56)   Grimme, S. Accurate Description of van der Waals Complexes by Density Functional Theory Including Empirical Corrections. *J. Comput. Chem.* **2004**, *25*, 1463–1473.

(57)   Grimme, S. Semiempirical GGA-Type Density Functional Constructed with a Long-Range Dispersion Correction. *J. Comput. Chem.* **2006**, *27*, 1787–1799.

(58)  Grimme, S.; Antony, J.; Ehrlich, S.; Krieg, H. A Consistent and Accurate Ab Initio Parametrization of Density Functional Dispersion Correction (DFT-D) for the 94 Elements H-Pu. *J. Chem. Phys.* **2010**, *132*, 154104 (1-18).

(59)  Civalleri, B.; Zicovich-Wilson, C. M.; Valenzano, L.; Ugliengo, P. B3LYP Augmented with an Empirical Dispersion Term (B3LYP-D*) as Applied to Molecular Crystals. *CrystEngComm* **2008**, *10*, 405–410.

(60)  Schäfer, A.; Horn, H.; Ahlrichs, R. Fully Optimized Contracted Gaussian-Basis Sets for Atoms Li to Kr. *J. Chem. Phys.* **1992**, *97*, 2571–2577.

(61)  Broyden, C. G. The Convergence of a Class of Double-Rank Minimization Algorithms. *J. Inst. Math. Its Appl.* **1970**, *6*, 76–90.

(62)  Fletcher, R. A New Approach to Variable Metric Algorithms. *Comput. J.* **1970**, *13*, 317–322.

(63)  Goldfarb, D. A Family of Variable Metric Updates Derived by Variational Means. *Math. Comput.* **1970**, *24*, 23–26.

(64)  Shanno, D. F. Conditioning of Quasi-Newton Methods for Function Minimization. *Math. Comput.* **1970**, *24*, 647–656.

(65)  Corno, M.; Ugliengo, P. Surface Modeling of Ceramic Biomaterials. In *Encycl. Nanotechnol.*; Bushan, B., Ed.; Springer Netherlands: Dordrecht, 2015; pp 1–13.

(66)  Jansen, H. B.; Ros, P. Non-Empirical Molecular Orbital Calculations on the Protonation of Carbon Monoxide. *Chem. Phys. Lett.* **1969**, *3*, 140–143.

(67)  Liu, B.; Mclean, A. D. Accurate Calculation of the Attractive Interaction of Two Ground State Helium Atoms. *J. Chem. Phys.* **1973**, *59*, 4557–4558.

(68)  Boys, S. F.; Bernardi, F. The Calculation of Small Molecular Interactions by the Differences of separate total energies. Some procedures with Reduced Errors. *Mol. Phys.* **1970**, *19*, 553–566.

(69)  Pascale, F.; Zicovich-Wilson, C. M.; Lopez Gejo, F.; Civalleri, B.; Orlando, R.; Dovesi, R. The Calculation of the Vibrational Frequencies of crystalline Compounds and its

Implementation in the CRYSTAL Code. *J. Comput. Chem.* **2004**, *25*, 888–897.

(70) Zicovich-Wilson, C. M.; Pascale, F.; Roetti, C.; Saunders, V. R.; Orlando, R.; Dovesi, R. The Calculation of the Vibration Frequencies of α-Quartz: The Effect of Hamiltonian and Basis Set. *J. Comput. Chem.* **2004**, *25*, 1873–1881.

(71) Tosoni, S.; Pascale, F.; Ugliengo, P.; Orlando, R.; Saunders, V. R.; Dovesi, R. Quantum Mechanical Calculation of the OH Vibrational Frequency in Crystalline Solids. *Mol. Phys.* **2005**, *103*, 2549−2558.

(72) Rimola, A.; Civalleri, B.; Ugliengo, P. Neutral vs Zwitterionic Glycine Forms at the Water/Silica Interface: Structure, Energies, and Vibrational Features from B3LYP Periodic Simulations. *Langmuir* **2008**, *24*, 14027−14034.

(73) Noël, Y.; Zicovich-Wilson, C. M.; Civalleri, B.; D'Arco, P.; Dovesi, R. Polarization Properties of ZnO and BeO: An Ab Initio Study through the Berry Phase and Wannier Functions Approaches. *Phys. Rev. B* **2001**, *65*, 0141(11-20).

(74) Williams, D. A. The Interstellar Medium: An Overview. In *Solid State Astrochemistry*; Pirronello, V., Krelowski, J., Manicò, G., Eds.; NATO Science Series, 2000; pp 1–20.

(75) Reuter, K.; Scheffler, M. Composition, Structure, And Stability of $RuO_2$ (110) as a function of oxygen pressure. *Phys. Rev. B* **2001**, *65*, 035406(1-11).

(76) Reuter, K.; Scheffler, M. Composition and Structure of the $RuO_2$ (110) Surface in an $O_2$ and CO Environment: Implications for the Catalytic Formation of $CO_2$. *Phys. Rev. B* **2003**, *68*, 045407(1-11).

(77) Digne, M.; Sautet, P.; Raybaud, P.; Euzen, P.; Toulhoat, H. Hydroxyl Groups on γ-Alumina Surfaces: A DFT Study. *J. Catal.* **2002**, *211*, 1–5.

(78) Digne, M.; Sautet, P.; Raybaud, P.; Euzen, P.; Toulhoat, H. Use of DFT to Achieve a Rational Understanding of Acid-Basic Properties of α-Alumina Surfaces. *J. Catal.* **2004**, *226*, 54–68.

(79) Bailey, C. L.; Wander, A.; Mukhopadhyay, S.; Searle, B. G. *Ab Initio Surface*

*Thermodynamics in Multi Component Environments*; 2007.

(80)    Bailey, C. L.; Mukhopadhyay, S.; Wander, A.; Searle, B. G.; Harrison, N. M. First principles Characterisation of Aluminium Trifluoride Catalysts. *J. Phys. Conf. Ser.* **2008**, *117*, 012004(1-8).

(81)    Bailey, C. L.; Mukhopadhyay, S.; Wander, A.; Searle, B. G.; Harrison, N. M. Structure and Stability of α-AlF$_3$ Surfaces. *J. Phys. Chem. C* **2009**, *113*, 4976–4983.

(82)    Mukhopadhyay, S.; Bailey, C. L.; Wander, A.; Searle, B. G.; Muryn, C. A.; Schroeder, S. L. M.; Lindsay, R.; Weiher, N.; Harrison, N. M. Stability of the AlF$_3$ (0 1 -1 2) surface in H$_2$O and HF Environments: An Investigation Using Hybrid Density Functional Theory and Atomistic Thermodynamics. *Surf. Sci.* **2007**, *601*, 4433–4437.

(83)    Wander, A.; Bailey, C. L.; Mukhopadhyay, S.; Searle, B. G.; Harrison, N. M. Steps, Microfacets and Crystal Morphology: An Ab Initio Study of β-AlF$_3$ Surfaces. *J. Phys. Chem.* **2008**, *112*, 6515–6519.

(84)    Rozanska, X.; Delbecq, F.; Sautet, P. Reconstruction and Stability of β-Cristobalite 001, 101, and 111 surfaces During Dehydroxylation. *Phys. Chem. Chem. Phys.* **2010**, *12*, 14930–14940.

(85)    Gierada, M.; Petit, I.; Tielens, F. Hydration in Silica Based Mesoporous Materials: A DFT Model. *Phys. Chem. Chem. Phys.* **2016**, *18*, 32962–32972.

(86)    Bostrom, D. Single-Crystal X-ray Diffraction Studies of Synthetic Ni–Mg Olivine Solid Solution. *Am. Mineral.* **1987**, *72*, 965–972.

(87)    Tasker, P. W. The Stability of Ionic Crystal Surfaces. *J. Phys. C Solid State Phys.* **1979**, *12*, 4977–4984.

(88)    Watson, G. W.; Oliver, P. M. Computer Simulation of the Structure and Stability of Forsterite Surfaces. *Phys. Chem. Miner.* **1997**, *25*, 70–78.

(89)    Escamilla-Roa, E.; Moreno, F. Adsorption of Glycine by Cometary Dust : Astrobiological Implications. *Planet. Space Sci.* **2012**, *70*, 1–9.

(90) Escamilla-Roa, E.; Moreno, F. Adsorption of Glycine on Cometary Dust Grains : II - Effect of Amorphous Water Ice. *Planet. Space Sci.* **2013**, *75*, 1–10.

(91) Wulff, G. Zur Frage der Geschwindigkeit des Wachstums und der Auflosung der Krystallflachen. *Zeitschrift für Kryst. und Mineral.* **1901**, *34*, 449–530.

(92) Momma, K.; Izumi, F. VESTA 3 for three-Dimensional Visualization of Crystal, Volumetric and Morphology Data. *J. Appl. Crystallogr.* **2001**, *44*, 1272–1276.

(93) Pilme, J.; Silvi, B.; Alikhani, M. E. Structure and Stability of M-CO, M = first-Transition-Row Metal: An application of Density Functional Theory and Topological Approaches. *J. Phys. Chem. A* **2003**, *107*, 4506–4514.

(94) Tiana, D.; Francisco, E.; Blanco, M. A.; Macchi, P.; Sironi, A.; Martín Pendás, A. Bonding in Classical and Nonclassical Transition Metal Carbonyls: The Interacting Quantum Atoms Perspective. *J. Chem. Theory Comput.* **2010**, *6*, 1064–1074.

(95) Bistoni, G.; Rampino, S.; Scafuri, N.; Ciancaleoni, G.; Zuccaccia, D.; Belpassi, L.; Tarantelli, F. How π Back-Donation Quantitatively Controls the CO Stretching Response in Classical and Non-Classical Metal Carbonyl Complexes. *Chem. Sci.* **2016**, *7*, 1174–1184.

(96) Goldman, A. S.; Krogh-Jespersen, K. Why Do Cationic Carbon Monoxide Complexes Have High C-O Stretching Force Constants and Short C-O Bonds? Electrostatic Effects, not σ-Bonding. *J. Am. Chem. Soc.* **1996**, *118*, 12159–12166.

(97) Lupinetti, A. J.; Fau, S.; Frenking, G.; Strauss, S. H. Theoretical Analysis of the Bonding between CO and Positively Charged Atoms. *J. Phys. Chem. A* **1997**, *101*, 9551–9559.

(98) Ferrari, A. M.; Ugliengo, P.; Garrone, E. Ab Initio Study of the Adducts of Carbon Monoxide with Alkaline Cations. *J. Chem. Phys.* **1996**, *105*, 4129–4139.

(99) Scuseria, G. E.; Miller, M. D.; Jensen, F.; Geertsen, J. The Dipole Moment of Carbon Monoxide. *J. Chem. Phys.* **1991**, *94*, 6660–6663 DOI: 10.1063/1.460293.

(100) Corno, M.; Busco, C.; Bolis, V.; Tosoni, S.; Ugliengo, P. Water Adsorption on the Stoichiometric (001) and (010) Surfaces of Hydroxyapatite: A Periodic B3LYP Study.

*Langmuir* **2009**, *25*, 2188–2198.

(101) Delle Piane, M.; Corno, M.; Ugliengo, P. Does Dispersion Dominate over H-Bonds in Drug-Surface Interactions? The Case of Silica-Based Materials as Excipients and Drug-Delivery Agents. *J. Chem. Theory Comput.* **2013**, *9*, 2404–2415.

(102) Ugliengo, P.; Garrone, E.; Ferrari, A. M.; Zecchina, A.; Otero Areán, C. Quantum Chemical Calculations and Experimental Evidence for O-Bonding of Carbon Monoxide to Alkali Metal Cations in Zeolites. *J. Phys. Chem. B* **1999**, *103*, 4839–4846.

(103) Bolis, V.; Fubini, B.; Garrone, E.; Giamello, E.; Morterra, C. A Comparison between the Lewis Acidity of non-D Metal Cations in Y-Zeolites and on Ionic Surfaces. *Stud. Surf. Sci. Catal.* **1989**, *48*, 159–166.

(104) Stecher, T. P.; Donn, B. On Graphite and Interstellar Extinction. *Astrophys. J.* **1965**, *142*, 1681–1683.

(105) Mathis, J. S.; Rumpl, W.; Nordsieck, K. H. The Size Distribution of Interstellar Grains. *Astrophys. J.* **1977**, *217*, 425–433.

(106) Draine, B. T.; Li, A. Infrared Emission from Interstellar Dust. I. Stochastic Heating of Small Grains. *Astrophys. J.* **2001**, *551*, 807–824.

(107) Li, A.; Draine, B. T. Infrared Emission from Interstellar Dust. II. The Diffuse Interstellar Medium. *Astrophys. J.* **2001**, *554*, 778–802.

(108) Draine, B. T. Interstellar Dust Grains. *Annu. Rev. Astron. Astrophys.* **2003**, *41*, 241–289.

(109) Cecchi-Pestellini, C.; Cacciola, A.; Iatì, M. a.; Saija, R.; Borghese, F.; Denti, P.; Giusto, A.; Williams, D. a. Stratified Dust Grains in the Interstellar Medium - II. Time-Dependent Interstellar Extinction. *Mon. Not. R. Astron. Soc.* **2010**, *408*, 535–541.

(110) Jones, A. P.; Fanciullo, L.; Köhler, M.; Verstraete, L.; Guillet, V.; Bocchio, M.; Ysard, N. The Evolution of Amorphous Hydrocarbons in the ISM: Dust Modelling from a New Vantage Point. *Astron. Astrophys.* **2013**, *558*, A62–A83.

(111) Larson, R. B. The Evolution of Molecular Clouds. In *The Structure and Content of*

*Molecular Clouds. 25 Years of Molecular Radioastronomy. Lecture Notes in Physics*; T.L., W., K.J., J., Eds.; Springer: Berlin, Heidelberg, 1994; Vol. 439, pp 13–28.

(112) Williams, J. P.; Blitz, L.; McKee, C. F. The Structure and Evolution of Molecular Clouds: from Clumps to Cores to the IMF. In *Protostars and Planets IV*; University of Arizona Press: Tucson, 1999.

(113) Jin, K.; Salim, D. M.; Federrath, C.; Tasker, E. J.; Habe, A.; Kainulainen, J. T. On the Effective Turbulence Driving Mode of Molecular Clouds Formed in Disc Galaxies. *Mon. Not. R. Astron. Soc.* **2017**, *469*, 383–393.

(114) Baba, J.; Morokuma-Matsui, K.; Saitoh, T. R. Eventful Evolution of Giant Molecular Clouds in Dynamically Evolving Spiral Arms. *Mon. Not. R. Astron. Soc.* **2017**, *464*, 246–263 DOI: 10.1093/mnras/stw2378.

(115) Corbelli, E.; Brain, J.; Bandiera, R.; Brouillet, N.; Combes, F.; Druard, C.; Gratier, P.; Mata, J.; Schuster, K.; Xilouris, M.; et al. From Molecules to Young Stellar Clusters: the Star Formation Cycle Across the M33 Disk. *Astron. Astrophys.* **2017**, *601*, A146–A163.

(116) Blyholder, G. Molecular Orbital View of Chemisorbed Carbon Monoxide. *J. Phys. Chem. A* **1964**, *68*, 2772–2777.

(117) Bolis, V.; Barbaglia, A.; Bordiga, S.; Lamberti, C.; Zecchina, A. Heterogeneous Nonclassical Carbonyls Stabilized in Cu (I) - and Ag (I) - ZSM-5 Zeolites: Thermodynamic and Spectroscopic Features. *J. Chem. Phys. B* **2004**, *108*, 9970–9983.

(118) Bolis, V.; Magnacca, G.; Morterra, C. Surface Properties of Catalytic Aluminas Modified by Alkaline-Earth Metal Cations: A Microcalorimetric and IR-Spectroscopic Study. *Res. Chem. Intermed.* **1999**, *25*, 25–56.

(119) Whittet, D. C. B.; Schutte, W. A.; Tielens, A. G. G. M.; Boogert, A. C. A.; de Graauw, T.; Ehrenfreund, P.; Gerakines, P. A.; Helmich, F. P.; Prusti, T.; van Dishoeck, E. F. An ISO SWS View of Interstellar Ices: First Results. *Astron. Astrophys.* **1996**, *315*, L357–L360.

(120) Mathis, J. S. Dust Models with Tight Abundance Constraints. *Astrophys. J.* **1996**, *472*, 643–

655.

(121) Mathis, J. S. The Near-Infrared Interstellar Silicate Bands and Grain Theories. *Astrophys. J.*
**1998**, *497*, 824–832.

**For TOC only**